Weakening Correlation and Delaying Response Time of Ecosystem Water Use Efficiency to Meteorological Drought

Zijun Wang[1], Rong Wu[2], Yangyang Liu[3], Zhaoying Zhang[4], Zhongming Wen[3], Zhenqian Wang[5], Stephen Sitch[6], Wenping Yuan[7]

Correspondence to: Yangyang Liu (hnlylcbtks@163.com)

[1] College of Water Resources and Architectural Engineering, Northwest A&F University, Yangling, Shaanxi 712100, China
[2] State Key Laboratory of Water Resources Engineering and Management, Wuhan University, Wuhan 430072, China
[3] College of Grassland Agriculture, Northwest A&F University, Yangling, Shaanxi 712100, China
[4] Jiangsu Center for Collaborative Innovation in Geographical Information Resource Development and Application, International Institute for Earth System Sciences, Nanjing University, Nanjing, Jiangsu 210023, China
[5] Department of Physical Geography and Bolin Centre for Climate Research, Stockholm University, Stockholm 10691, Sweden
[6] Faculty of Environment, Science and Economy, University of Exeter, Exeter, UK
[7] Institute of Carbon Neutrality, Sino-French Institute for Earth System Science, College of Urban and Environmental Sciences, Peking University, Beijing, China

Abstract: Ecosystem water use efficiency (WUE), defined as the ratio of ross primary production (GPP) to evapotranspiration (ET), representing the balance between carbon gain and water loss,~~carbon gain to water loss,~~ is significantly affected by meteorological drought. Understanding the coupling relationship between WUE and drought has been a central focus of global research. Currently, the coupling relationship is primarily assessed using correlation coefficients or linear regression slopes. However, the optimal drought timescale at which WUE responds to drought, a key indicator of vegetation sensitivity, has largely been overlooked. ~~Elucidating the coupling relationship between WUE and drought is essential for understanding the carbon–water trade-off strategies of vegetation under drought stress. Most existing studies mainly evaluated coupling relationship using correlation coefficients or regression slopes. However, the optimal drought timescale governing WUE responses to drought has not yet been systematically investigated.~~ Therefore,~~To fill these gaps,~~ this study investigated the spatiotemporal patterns of the WUE - meteorological drought ~~drought~~ coupling relationship ~~(characterized by the maximum correlation coefficient, R_{max}, and optimal lag time, T_{opt})~~ across global terrestrial ecosystems from 1982 to 2018 with satellite-derived and model-simulated WUE, together with the Standardized Precipitation–Evapotranspiration Index (SPEI), and ~~further~~ explored the potential causal mechanisms using hydrometeorological data. The results indicated that maximum correlation coefficient between WUE and SPEI decreased at a rate of -0.0003/year, while the optimal drought timescale increased at a rate of 0.0155 months/year, suggesting weakened sensitivity and delayed response time of WUE to meteorological drought.~~revealed a delaying of the drought response timescale of WUE, accompanied by a weakening in the WUE–drought correlation at the optimal timescale, as evidenced by a decrease in R_{max} at a rate of -0.0003/year and an increase in T_{opt} at a rate of 0.0155 months/year, indicating a globally weakened coupling relationship.~~ ~~Moreover, pronounced heterogeneity in the changes of coupling relationships changes was observed across different drought gradients and vegetation types.~~ Attribution analysis indicated that CO_2 fertilization was the primary factor contributing to the weakening of the coupling relationship. Surface soil moisture ~~(SMsurf)~~ was the most critical hydrometeorological ~~hydrothermal~~ driver, exhibiting nearly opposite effects and significant threshold effects on maximum correlation coefficient and optimal drought timescale~~R_{max} and T_{opt}~~. Causality diagnosis framework was further employed to construct direct and indirect causal networks between ~~of~~ hydrometeorological ~~hydrothermal~~ factors and coupling relationship~~affecting R_{max} and T_{opt} across different vegetation types and drought gradients~~. The results showed that the decrease in the maximum correlation coefficient had direct negative causal effects on precipitation, temperature, and radiation. In contrast, the increase in the optimal drought timescale was primarily driven by a negative causal effect of radiation and a positive causal effect of wind speed, and in turn exerted direct positive and negative causal effects on precipitation and temperature, respectively. This study highlights the weakened coupling between WUE and meteorological drought, suggesting that vegetation's carbon-water trade-off is evolving toward drought adaptation, which is crucial for understanding the adaptive strategies of vegetation in response to climate change.

Short summary:

Ecosystem water use efficiency exhibited a reduced correlation with drought and a delayed response timing from 1982 to 2018, a pattern primarily driven by CO_2 fertilization. Surface soil moisture emerged as the dominant hydroclimatic driver, exerting contrasting influences and exhibiting pronounced threshold effects. This study highlights the divergent vegetation adaptation strategies across arid and humid regions, underscoring the need to reassess the water use efficiency–drought relationship.

Keywords:

Water Use Efficiency (WUE), Standardized Precipitation-Evapotranspiration Index (SPEI), Coupling relationship, Dynamic Global Vegetation Models (DGVMs), Machine learning, Causal diagnosis

1. Introduction

Ecosystem water use efficiency (WUE) is defined as~~refers to~~ the ratio of carbon assimilation to ecosystem water evapotranspiration (Beer et al., 2009). ~~A high~~High WUE indicates that an ecosystem can more effectively carry out photosynthesis and growth under limited water resources (Wang et al., 2022). Therefore, the WUE is widely used to characterize the trade-off between carbon uptake and water loss within ecosystems~~the interactions between the carbon and water cycles within ecosystems is often quantified using WUE~~ (Xue et al., 2022). Meteorological drought, as one of the most common and destructive natural hazards, plays a critical role in altering terrestrial carbon–water cycles (Li et al., 2026). Against the backdrop of global climate change, the frequency, duration, and intensity of meteorological drought are projected to continue increasing in the future (Mokhtar et al., 2021; Trenberth et al., 2014; Chen et al., 2023), which will have increasingly profound effects on terrestrial ecosystems. Therefore, understanding the impacts of meteorological drought on terrestrial carbon–-water dynamics is of great significance for ecosystem sustainability (Wang et al., 2026a).

Previous studies have shown that WUE responses to drought exhibit significant spatiotemporal heterogeneity. Across aridity gradients, WUE exhibits a negative response to drought in arid ecosystems, whereas it shows a positive response in humid ecosystems (Huang et al., 2017). From a temporal perspective of drought development, WUE decreases during summer droughts but increases during autumn droughts (Ma et al., 2019). Furthermore, WUE demonstrates a two-phase relationship with drought intensity: increasing under moderate drought but declining under severe drought (Lu and Zhuang, 2010). The timing of drought occurrence also plays a crucial role in regulating both the direction and magnitude of WUE responses, as ecosystem physiological and physical processes exhibit varying sensitivities to water stress across different growth stages (Huang et al., 2021; Wang et al., 2021).

~~Drought, as one of the major natural disturbances affecting ecosystems, plays a critical role in regulating carbon uptake and transpiration. Drought can constrain vegetation growth (Jiao et al., 2021; Wu et al., 2025), and even trigger widespread vegetation mortality, thereby disrupting terrestrial carbon balance (Reichstein et al., 2013; Schwalm et al., 2012). Previous studies have investigated the impacts of drought on WUE from multiple perspectives. Some studies have focused on the effects of drought events on WUE (Huang et al., 2017; Ma et al., 2019; Xie et al., 2016; Zhao et al., 2022). For example, Huang et al. (2017) identified contrasting WUE responses to drought stress, with negative responses in arid ecosystems but positive responses in humid ecosystems. Ma et al. (2019) found that in young Forest in northern China, drought reduced WUE in summer but enhanced it in autumn. Xie et al. (2016) reported similar patterns, showing that drought during the leaf expansion stage reduced WUE, whereas drought during the leaf discoloration stage increased WUE. In addition, Zhao et al. (2022), in their study of alpine meadows on the Tibetan Plateau, observed that drought led to an increase in WUE in the early growing season, but a decrease in mid-season WUE. Other studies have emphasized the relationships between drought characteristics and WUE (Lu and Zhuang, 2010; Huang et al., 2021; Wang et al., 2021; Li et al., 2022a). For instance, Lu and Zhuang (2010) identified a two-phase relationship between WUE and drought intensity, whereby WUE increased under moderate drought but declined under severe drought. The timing of drought occurrence also plays a crucial role in regulating both the direction and magnitude of WUE responses, as ecosystem physiological and physical processes exhibit varying sensitivities to water stress across different growth stages (Huang et al., 2021; Wang et al., 2021). Moreover, Li et al. (2022a) demonstrated that WUE increased as drought intensity weakened. Because WUE at different scales represents distinct carbon–water cycling processes, several studies have examined scale-dependent drought responses of WUE (Yang et al., 2025; Poppe Terán et al., 2023; Li et al., 2025). A recent pan-European analysis showed that ecosystem WUE predominantly responded negatively to drought, whereas intrinsic WUE (IWUE, defined as the ratio of GPP to canopy conductance) exhibited positive responses across more than 90% of Europe (Poppe Terán et al., 2023). Yang et al. (2025) examined the directional responses of multi-scale WUE to drought and found that during drought periods, transpiration WUE (TWUE, defined as GPP divided by transpiration) declined, ecosystem WUE showed no clear directional change, and underlying WUE (uWUE, defined as WUE multiplied by the square root of vapor pressure deficit) increased. Using a conceptual drought propagation framework, Li et al. (2025) further demonstrated that although IWUE increased during drought, ecosystem WUE declined, indicating that stomatal regulation operates primarily at the leaf level and cannot fully offset drought-induced reductions in ecosystem-scale WUE.~~

However, these studies remain limited, as they have largely been conducted at specific or fixed drought timescales, thereby neglecting the cumulative and lagged effects of drought on vegetation dynamics. ~~In recent years, increasing attention has been paid to characterizing temporal changes in vegetation responses to drought, with most studies reporting an increasing sensitivity of vegetation to drought (Jiao et al., 2021; Li et al., 2022b; Zhang et al., 2022). However, these studies were largely~~

~~conducted at specific or fixed drought timescales, neglecting the cumulative and lagged effects of drought on vegetation dynamics (Wen et al., 2019), and primarily relied on single indicators such as gross primary productivity (GPP), which represents photosynthetic activity, or vegetation indices that reflect canopy greenness. In contrast, ecosystem WUE provides a more integrative measure of vegetation carbon–water trade-off strategies under water stress.~~ In fact, plants can uptake water stored from past precipitation in deeper unsaturated soil layers or groundwater to maintain carbon–water balance (Zhang et al., 2026).~~It is widely acknowledged that~~ In other words, drought not only impacts vegetation growth synchronously but also exhibits lagged and cumulative effects, where past drought conditions influence current vegetation growth (Huang et al., 2018; Kannenberg et al., 2020). Vicente-Serrano et al. (2013) emphasized that vegetation responses to drought are inherently multi-timescale in nature. Longer timescales imply stronger memory effects, which may buffer the impacts of recent drought events and thereby reduce vegetation drought sensitivity (Seddon et al., 2016). In contrast, shorter timescales indicate more rapid vegetation responses to moisture deficits, reflecting higher drought sensitivity (Jiao et al., 2021). Therefore, neglecting the role of timescales in assessing WUE-drought coupling may hinder our understanding of how WUE responds to drought. Despite the growing body of literature on WUE responses to drought, few studies have examined the coupling relationship between WUE and drought, particularly from a multi-timescale perspective. Therefore, incorporating multi-timescale drought effects into analyses of WUE–drought coupling is essential for a more comprehensive and accurate understanding of vegetation carbon–water trade-offs under drought stress.

Therefore, we calculated the coupling relationship between WUE and SPEI across time scales ranging from 1 to 24 months, including the maximum correlation coefficient (R_{max}) and optimal drought timescale~~optimal lag time~~ (T_{opt}). Subsequently, we utilized Dynamic Global Vegetation Models from TRENDY project to quantify the contributions of CO_2, climate change (CLI), and land-use change (LCC) to this coupling relationship. To further explore the impact of climate change, we employed the eXtreme Gradient Boosting (XGBoost) algorithm combined with SHapley Additive Explanations (SHAP) to identify both the relative importance and modes of influence of key hydrothermal factors in shaping the coupling relationship between WUE and drought. Finally, we employed Peter-Clark Momentary Conditional Independence Plus (PCMCI+) to uncover the complex causal network between hydrothermal factors, R_{max}, and T_{opt}. These findings are expected to enhance our understanding of the vulnerability of terrestrial ecosystems to drought and provides valuable insights for supporting ecosystem sustainability under climate change.

2. Data sources and processing

2.1. GPP and ET data

Three widely used GPP datasets were employed in this study: FLUXCOM GPP, GLASS GPP, and NIRv GPP. FLUXCOM GPP, which is derived from a machine learning-based integration of eddy covariance measurements and remote sensing data, offers global coverage with monthly temporal resolution and a spatial resolution of 0.5°. The GLASS GPP product, generated using a light use efficiency model in conjunction with AVHRR reflectance data, provides 8-day composite estimates with a spatial resolution of 0.5° from 1982 - 2018. To aggregate the 8-day time-scale GPP data into monthly values, the maximum value method was utilized. NIRv GPP, a recently developed satellite-derived index based on near-infrared reflectance of vegetation, features a monthly temporal resolution and a 0.05° spatial resolution, and exhibits a strong correlation with tower-based GPP measurements. These datasets collectively represent distinct methodological approaches to quantifying terrestrial carbon uptake while maintaining complementary spatiotemporal characteristics suitable for cross-comparison analysis.

Three widely used ET datasets were analyzed in this study: ERA5 ET, GLASS ET, and GLEAM ET. ERA5 ET, produced by the European Centre for Medium-Range Weather Forecasts through atmospheric reanalysis modeling, provides monthly temporal resolution at a 0.25° spatial grid, incorporating land-atmosphere interaction processes. The AVHRR-based GLASS ET data employs the Bayesian Model Averaging method, which merges five process-based ET algorithms to improve ET estimation. It provides ET data spanning from 1981 to 2022 with an 8-day temporal resolution and a 0.5° spatial resolution. In GLEAM, multiplicative evaporative stress factors are applied to convert the estimated potential evapotranspiration values of three land components—bare soil, high-canopy, and short-canopy—into bare soil evaporation (Eb) and transpiration (Et). Interception loss (Ei) is calculated separately using an analytical model driven by precipitation and vegetation characteristics. The actual evapotranspiration is estimated as the sum of these three components. GLEAM ET provides data with a monthly temporal resolution and a 0.25° spatial resolution. These datasets collectively represent diverse retrieval approaches (reanalysis, hybrid model, and observation-driven algorithm) while maintaining spatially and temporally complementary resolutions, enabling robust intercomparison of terrestrial water flux patterns across multiple scales.

~~Furthermore, WUE is calculated as the ratio of GPP to ET according to Equation (1):~~

~~$$WUE = GPP/ET \quad (1)$$~~

~~In this study, based on these three independent sets of GPP products and three sets of ET products, we first computed WUE for each GPP-ET product combination. Then, we integrated the results of the nine WUE combinations using an arithmetic mean, ultimately generating a multi-product averaged WUE. This approach effectively reduces the impact of systematic errors from individual products, thereby enhancing the robustness of the estimated results (Wu et al., 2025).~~

2.2. FLUXNET data

To validate the reliability of WUE data observed from multi-source satellite~~remote sensing~~ products, this study collected flux data from FLUXNET 2015 (https://fluxnet.org/). To ensure the long-term reliability of WUE observations, we selected sites with continuous observation records of more than 5 years and with complete and valid records were selected. Based on this criterion, 85 flux stations were ultimately selected for analysis at the monthly scale (Figure S1, Table S1). Among these sites, only high-quality gap-filled data (QC > 0.8) were retained (Guan et al., 2025). Additionally, to ensure the accuracy of ET estimates, the energy balance closure criterion was applied: when the energy imbalance (net radiation minus the sum of latent heat flux, sensible heat flux, and soil heat flux) exceeded 50% of the available energy, the latent heat flux (LE) was treated as missing (Knauer et al., 2018). GPP was estimated using the nighttime respiration allocation method ("GPP_NT_VUT_REF") to ensure consistency across sites.

~~Representative long-term scale sites from different land use types were selected, and remote sensing products were compared with ground-based flux measurements. In the calculation of WUE, GPP can be directly obtained, while ET is computed using the Equation (2):~~

$$ET = \frac{LE}{2.501 - 2.361 \times 10^{-3} \times T} \quad (2)$$

~~where ET represents actual evapotranspiration (mm/month), LE (W/m²) represents latent heat flux, and T (°C) is the air temperature.~~

~~To ensure the long-term reliability of WUE observations, we selected sites with continuous observation records of more than 5 years, all with valid data. Based on this criterion, we ultimately selected 85 flux stations for analysis at the monthly scale (Figure S1, Table S1). The validation results indicated a high correlation between satellite-based WUE and the flux-based WUE (R = 0.62, Figure S2), implying that satellite-based WUE results were very robust.~~

2.3. TRENDY v12 multi-model simulated GPP and ET data

The latest version TRENDY v12 (Trends in Net Land-Atmosphere Carbon Exchange) is a collaborative initiative that integrates multiple Dynamic Global Vegetation Models (DGVMs) (https://blogs.exeter.ac.uk/trendy), aimed at quantifying global carbon budgets using forcing data on carbon dioxide concentrations, climate variables, and land use changes (Friedlingstein et al., 2023). All models utilize the same forcing data, with historical climate fields derived from the CRUv.4.07 and CRU-JRA55 datasets, and global atmospheric CO_2 concentrations obtained from a combination of ice core records and atmospheric observations. Each DGVM model runs four simulation scenarios: S0 (no changes in CO_2, climate, or land cover), S1 (changes in CO_2, static climate conditions, and static land use), S2 (changes in CO_2 and climate conditions, static land use), and S3 (changes in CO_2, climate conditions, and land use).

2.4. SPEI data

The SPEI is commonly used to assess climate drought conditions. By incorporating regional precipitation, potential evapotranspiration, and temperature, the SPEI quantifies the hydrological balance over a specific period and provides an objective method for comparing drought severity across different regions and time periods. It is of considerable importance for monitoring and predicting the impact of climate change on water resources and ecosystems. To ensure consistency with the climate data version used in the TRENDY model (CRU TS 4.07), we selected the SPEI version 2.9 dataset, which is derived from CRU TS 4.07 (https://spei.csic.es/spei_database). This dataset has a spatial resolution of 0.5° × 0.5° and covers timescales ranging from 1 to 24 months (Beguería et al., 2014).

2.5. Hydrometeorological ~~Hydrothermal~~ factors data

Since CRU climate data (CRUts4.07 and CRU-JRA55) is widely used as climate forcing in DGVMs, we adopt the same climate factor data in this study to ensure consistency with these models. Specifically, we collected monthly mean temperature (Temp), precipitation (Pre), and actual vapor pressure data (V_{ap}) from the CRUts4.07 climate product, as well as downward shortwave radiation (Rad) and wind speed (WS) data from the CRU Japanese Reanalysis (CRU JAR) (https://crudata.uea.ac.uk/). Soil moisture data for the surface layer (0-10 cm, SMsurf) and root zone (10-100 cm, SMroot) were obtained from the Global Land Evaporation Amsterdam Model (GLEAM) (https://www.gleam.eu/). Additionally, the vapor pressure deficit (VPD) was calculated based on monthly average temperature and actual vapor pressure using the following Equation (Wang et al., 2025):

$$\lg E_w = C_1 \times \left(1 - \frac{T_1}{T}\right) + C_2 \times \lg\left(\frac{T}{T_1}\right) + C_3 \times \left[1 - 10^{C_6 \times \left(\frac{T}{T_1} - 1\right)}\right] + C_4 \times \left[10^{C_7 \times (1 - T_1/T)} - 1\right] + C_5 \quad (3\text{1})$$

$$\mathrm{VPD} = E_w - V_{ap} \quad (4\text{2})$$

Where, E_w represents the saturated vapor pressure. and V_{ap} represents the actual vapor pressure. The constants used are as follows: $C_1 = 0.1079574 \times 10^2$, $C_2 = -0.5028 \times 10$, $C_3 = 0.150475 \times 10^3$, $C_4 = 0.42873 \times 10^{-3}$, $C_5 = 0.78614$, $C_6 = -0.82969 \times 10$, $C_7 = 0.476955 \times 10$. Additionally, $T_1 = 273.16\mathrm{K}$ (the triple point temperature of water), and $T = 276.15 + \mathrm{t(K)}$, where t is the air temperature in Celsius.

2.6. Land use types data

This study utilizes the annual HLDA+ Global Land Use Change dataset (https://doi.pangaea.de/10.1594/PANGAEA.921846), which includes six general land use/cover categories: urban areas, croplands, pastures/rangelands, Forest, unmanaged grasslands/shrublands, and sparse/bare soils. We excluded pixels with land

use types of "urban areas" and "sparse/bare soils" to define permanent vegetation areas (Winkler et al., 2021), and all subsequent studies were conducted within these permanent vegetation areas (Figure S4).

2.7. Aridity index data

Using the third edition of the Global Aridity Index and Potential Evapotranspiration dataset (Global-AI-PET-v3, https://doi.org/10.6084/m9.figshare.7504448.v5), the globe is classified into four aridity gradients based on the following thresholds: AI < 0.2 as arid (AR), 0.2 ≤ AI < 0.5 as semi-arid (SAR), 0.5 ≤ AI < 0.65 as dry sub-humid (DSH), and AI > 0.65 as humid (HU) (Figure S3).

2.8. Pre-processing

All datasets were resampled to a spatial resolution of 0.25° using bilinear interpolation (Li et al., 2022c). Moreover, seasonal cycles and long-term trends in WUE and SPEI data may lead to spurious correlations (Boulton et al., 2022). Therefore, it is essential to perform deseasonalization and detrending on WUE and SPEI prior to subsequent calculations (Smith and Boers, 2023). This study employed the Seasonal and Trend decomposition using Loess (STL) method to decompose WUE and SPEI time series of each grid cell into the overall trend, seasonal component, and residual component, as implemented using the *stl()* function in the "stats" package in R (v4.2.1). The STL residual component, which represents the deseasonalized and detrended WUE and SPEI time series, were utilized for further analysis (Wang et al., 2023).

3. Methods

3.1. Definition of WUE

The grid-scale ecosystem WUE was calculated as the ratio of GPP to ET according to equation (3):

$$WUE = GPP/ET \quad (3)$$

Where, the unit of WUE is gC·m^{-2}·month^{-1}, the unit of GPP is gC·m^{-2}·month^{-1}, and the unit of ET is mm^{-1} month^{-1}. In this study, based on these three independent sets of GPP products and three sets of ET products, we first computed WUE for each GPP-ET product combination. Then, we integrated the results of the nine WUE combinations using an arithmetic mean, ultimately generating a multi-product averaged WUE. This approach effectively reduces the impact of systematic errors from individual products, thereby enhancing the robustness of the estimated results (Wu et al., 2025).

Representative long-term scale sites from different land use types were selected were selected to validate the satellite products. In the calculation of site-scale ecosystem WUE, GPP can be directly obtained, while ET is computed using the equation (4):

$$ET = \frac{LE}{2.501 - 2.361 \times 10^{-3} \times T} \quad (4)$$

where ET represents actual evapotranspiration (mm/month), LE (W/m²) represents latent heat flux, and T (°C) is the air temperature. The validation results indicated a high correlation between satellite-based WUE and the flux-based WUE (R = 0.62, Figure S2), implying that satellite-based WUE results were highly reliable.

3.~~1~~2. Calculation of coupling relationship between WUE and drought

~~Vicente-Serrano et al. (2013) showed that R_{max} and T_{opt} are reliable indicators of the vegetation-drought coupling. The T_{opt}, which reflects vegetation's response to drought, is determined by identifying the time scale at which R_{max} occurs between WUE and SPEI (Vicente-Serrano et al., 2012). Specifically, for each pixel, the WUE time series (1-12 months) is compared to the corresponding SPEI series, spanning time scales from 1 to 24 months. The highest value among the 288 correlation coefficients (12 months × 24 time scales) is retained for each pixel, and the corresponding SPEI time scale is defined as T_{opt} (Li et al., 2024).~~

The coupling relationship was defined as the maximum correlation coefficient (R_{max}) and optimal lag time (T_{opt}) between WUE and SPEI. In general, WUE decreases with increasing drought severity, whereas it tends to be higher under mild or non-drought conditions (Li et al., 2025) , indicating an overall positive correlation between WUE and SPEI. Accordingly, R_{max} was defined as the maximum (non-absolute) correlation coefficient between SPEI at different time scales and WUE, representing the maximum sensitivity of WUE to SPEI (Vicente-Serrano et al., 2012). SPEI typically exhibits a lagged effect on WUE, whereby past drought conditions influence current WUE (Huang et al., 2018; Kannenberg et al., 2020) Therefore, T_{opt} was defined as the SPEI time scale corresponding to R_{max}, representing the response time of WUE to SPEI (Li et al., 2024).

3.~~2~~3. Trend analysis

An 18-year moving window was employed to investigate the temporal variations in R_{max} and T_{opt} over the past four decades. Then, we utilized a combination of Theil-Sen slope estimation and the Mann-Kendall (MK) test to identify and analyze trends in long-term time series data. The Theil-Sen method was applied to calculate robust linear trends, with p-values that remain resilient to the influence of outliers (Gocic and Trajkovic, 2013). At the same time, the non-parametric MK test was employed to assess the significance of monotonic trends by evaluating their slope values (Ma et al., 2020). To ensure the robustness of the identified temporal trends, we further examined the trends of R_{max} and T_{opt} using 16-year and 20-year moving windows~~by varying the width of the moving window~~.

3.~~3~~4. Attribution analysis and causality diagnosis of WUE-drought coupling relationship

We compared the coupling relationships derived from the simulation results of all DGVMs under the S3 scenario with those calculated from remote sensing observations, and ultimately retained only the seven models that were consistent with the remote sensing results: E3SM, EDv3, JSBACH, JULES, LPJ-GUESS, SDGVM, and VISIT (Zeng et al., 2022) ~~(Figure S6)~~. We not only computed WUE for each individual model but also calculated the multi-model mean WUE under the S1, S2, and S3 scenarios (Figure S6). Furthermore, we derived R_{max} and T_{opt} to examine the relationship between WUE and SPEI. Considering that the coupling relationship under the S1 scenario can only represent the effects of CO_2 changes, we also computed the coupling relationships for the (S2 - S1) and (S3 - S2) scenarios to quantify the contributions of CLI and LCC to the changes in R_{max} and T_{opt}.

Machine learning models are capable of effectively capturing the nonlinear relationships between multidimensional predictors and target variables (Yan et al., 2025b). With the advancement of interpretability techniques such as SHapley Additive Explanations (SHAP), machine learning has gradually evolved from a black-box paradigm into an explainable artificial intelligence framework. Therefore, to complement our understanding of CLI, this study selected a series of hydrometeorological ~~hydrothermal~~ factors—including VPD, SMsurf, SMroot, Temp, Pre, WS, and Rad—and employed the XGBoost algorithm to quantify their respective influences on R_{max} and T_{opt} (Piao et al., 2020). To increase the sample size, all time-series data from each grid cell were extracted. The dataset was divided into training and test ~~testing~~ subsets at a ratio of 80:20. Bayesian optimization combined with five-fold cross-validation was used for hyperparameter tuning~~,~~. For the R_{max} model, the learning rate was set to 0.06, the number of trees to 1431, and the maximum depth to 4. For the T_{opt} model, the learning rate was set to 0.07, the number of trees to 1287, and the maximum depth to 4. The ~~and~~ model performance was evaluated using the mean coefficient of determination (R^2) and root mean square error (RMSE) obtained through five-fold cross-validation (Figure S19).

This study further employed the improved Peter-Clark Momentary Conditional Independence plus algorithm (PCMCI+) (Runge et al., 2019; Runge, 2020) to investigate the causal mechanisms between R_{max} and T_{opt}, and hydrometeorological~~hydrothermal~~ factors. This method introduced three key optimizations to the classical PCMCI framework: (1) enhancing traditional Granger causality, which focuses solely on lagged effects, by incorporating momentary causality detection; (2) adopting a mixed conditioning set strategy to improve computational efficiency in high-dimensional datasets; and (3) refining false discovery rate (FDR) correction methods to enhance the reliability of causal networks. Specifically, the analytical process comprised two interdependent stages. In the first stage, an adaptive PC algorithm was employed to simultaneously select variables and determine lag orders, utilizing an information entropy-based variable importance assessment to dynamically construct the "candidate causal set" for each target variable. In the second stage, an improved

Momentary Conditional Independence (MCI) test was conducted, which not only considered traditional lagged causality ($\tau \leq 5$) but also incorporated momentary causality ($\tau = 0$). Instead of the conventional ParCorr method, a Gaussian process-based nonlinear conditional independence test (GPDC) was applied, and p-values were computed through permutation testing (500 bootstrap iterations), with significance determined using an FDR-corrected threshold of $p < 0.05$.

4. Results

4.1. Spatiotemporal Characteristics of R_{max} and T_{opt}

Based on remote sensing observations and the TRENDY multi-model ensemble, we computed the R_{max} and T_{opt} trends between ecosystem WUE and drought (Figure 1). The results indicated that the R_{max} derived from both datasets declined significantly at a rate of -0.0003/year ($p<0.01$)~~, which was consistent with our observations under the 16-year and 20-year moving window analyses (Figure S5)~~. Furthermore, the T_{opt} calculated from remote sensing observations and the TRENDY multi-model ensemble increased at rates of 0.0155 months/year and 0.0222 months/year ($p<0.01$), respectively. Notably, the R_{max} derived from the TRENDY multi-model ensemble were approximately 0.02 lower than those from remote sensing observations, whereas the T_{opt} were about 0.5 months higher; however, both datasets exhibited nearly identical temporal trends.

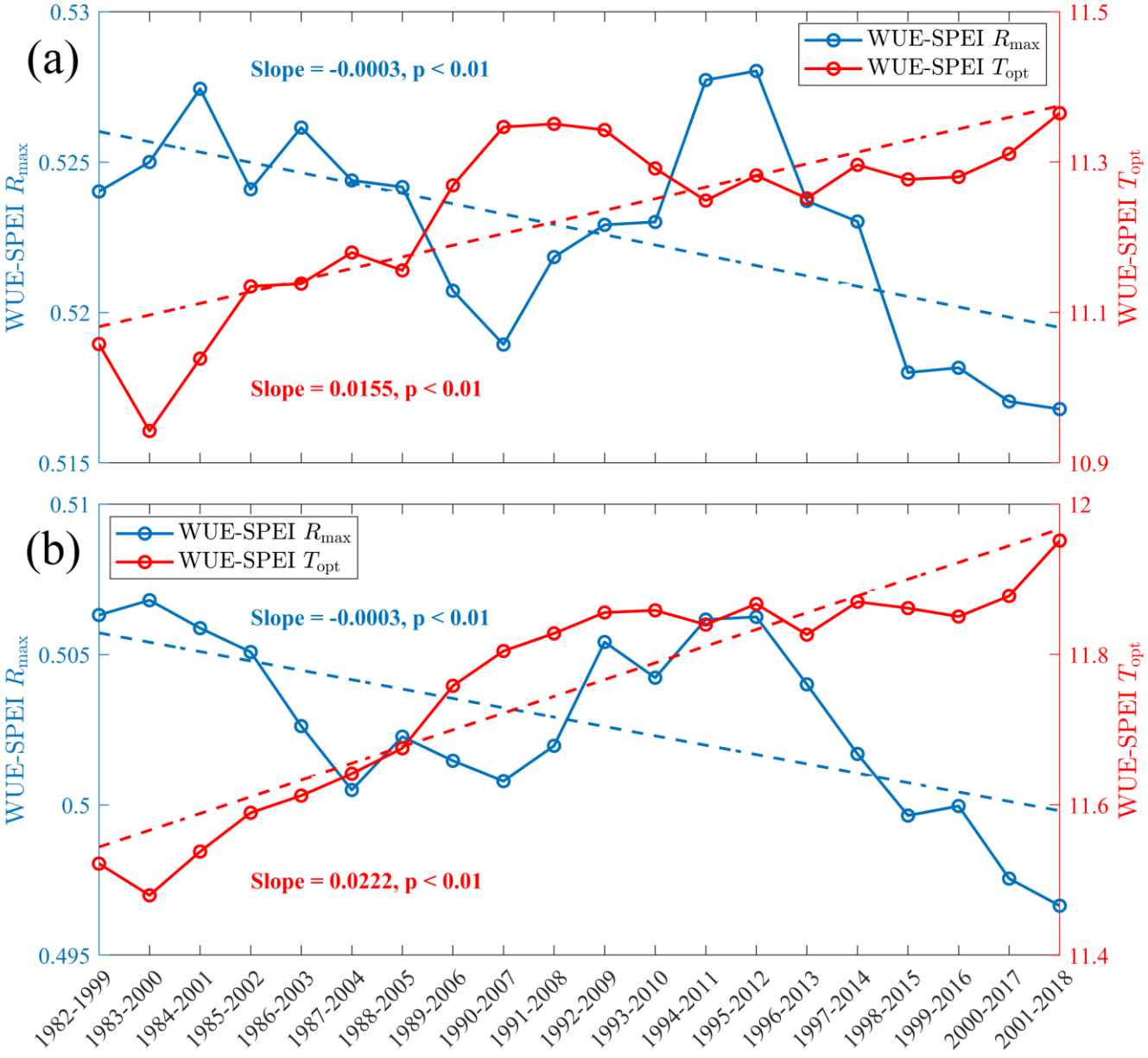

Figure 1. Temporal trends of the R_{max} and T_{opt} between global WUE and SPEI calculated from (a) the remote sensing observations and (b) the TRENDY multi-model ensemble using an 18-year moving window.

The spatial patterns of the multi-year mean values and trends of R_{max} and T_{opt} were generally consistent, although the R_{max} derived from the TRENDY multi-model ensemble was smaller and the T_{opt} was larger than those obtained from remote sensing observations (Figure 2). It was also noteworthy that the absolute values of the R_{max} and T_{opt} trends estimated from remote sensing observations were slightly larger than those derived from the TRENDY multi-model ensemble. ~~Similar patterns were also observed in the 16-year and 20-year moving window analyses (Figures S7–S11).~~ Specifically, in the high-latitude regions of the Northern Hemisphere, the R_{max} generally showed a decreasing trend, with the exception of the western Siberia, and central North America~~Chersky Mountains, the West Siberian Plain, and the North American Great Plains~~. Notably, the decrease was most pronounced in the ~~Central~~ central Siberian ~~Plateau~~. In contrast, the Southern Hemisphere exhibited more regions where the R_{max} have increased, particularly in areas such as the central-northern Africa ~~Chad Basin~~, southern Africa,

northern Australia, and the Amazon Basin, where the increasing rate was notably high. The T_{opt} exhibited an opposite trend to the R_{max}, showing a clear increase between 30°N and 60°N, while the remaining regions primarily exhibited a decreasing trend.

From the perspectives of vegetation type and drought gradient, the mean values of R_{max} and T_{opt} showed relatively small differences, whereas their trends exhibited pronounced heterogeneity across these two dimensions (Figure 2c). Specifically, the mean R_{max} varied little across aridity gradients~~drought gradients~~ but differed among vegetation types, with Shrub showing higher mean values than other vegetation types, particularly Shrub in HR, which reached 0.54. The mean characteristics of T_{opt} were consistent with those of R_{max}, with the highest mean T_{opt} observed in HR across aridity gradients~~drought gradients~~ and among shrubs across vegetation types. In terms of the rate of change, R_{max} showed an overall decreasing trend globally but increased in AR, with the highest growth rates observed in Forest and Shrub, at 0.0017/year and 0.0021/year, respectively. Across vegetation types, R_{max} also tended to increase in Pasture. In contrast, the rate of change in T_{opt} showed marked regional differences across aridity gradients~~drought gradients~~, with higher increasing rates in AR, reaching up to 0.1181 months/year in Pasture, while SH showed a decreasing trend at –0.0010 months/year. Across vegetation types, T_{opt} increased more rapidly in Cropland and Pasture, whereas Forest displayed a decreasing trend, with the largest decline occurring in Forest within SAR at –0.0394 months/year.

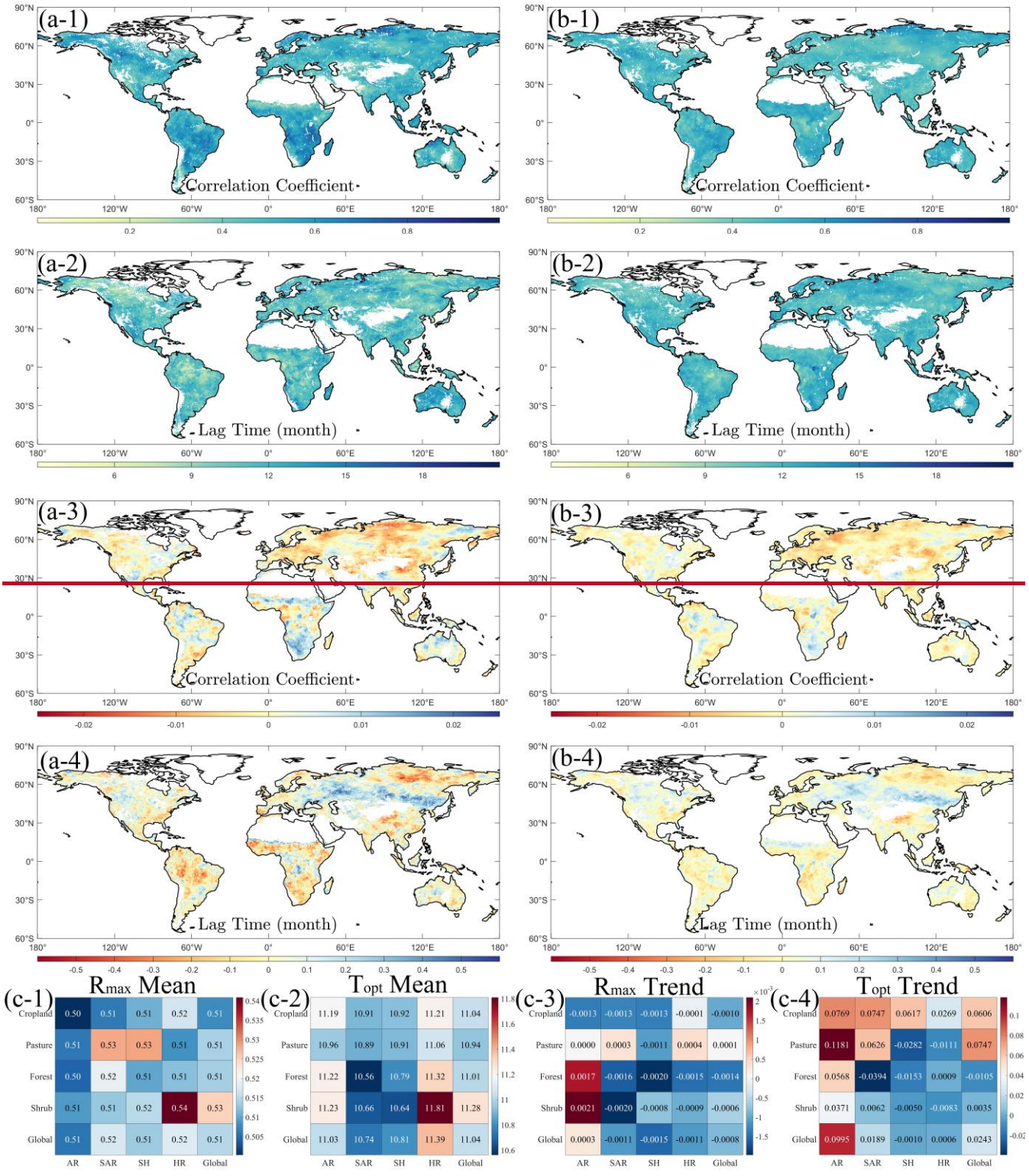
(a-1)
Correlation Coefficient
(b-1)
Correlation Coefficient
(a-2)
Lag Time (month)
(b-2)
Lag Time (month)
(a-3)
Correlation Coefficient
(b-3)
Correlation Coefficient
(a-4)
Lag Time (month)
(b-4)
Lag Time (month)
(c-1) Rmax Mean
(c-2) Topt Mean
(c-3) Rmax Trend
(c-4) Topt Trend
Cropland
Pasture
Forest
Shrub
Global
AR
SAR
SH
HR
Global

337

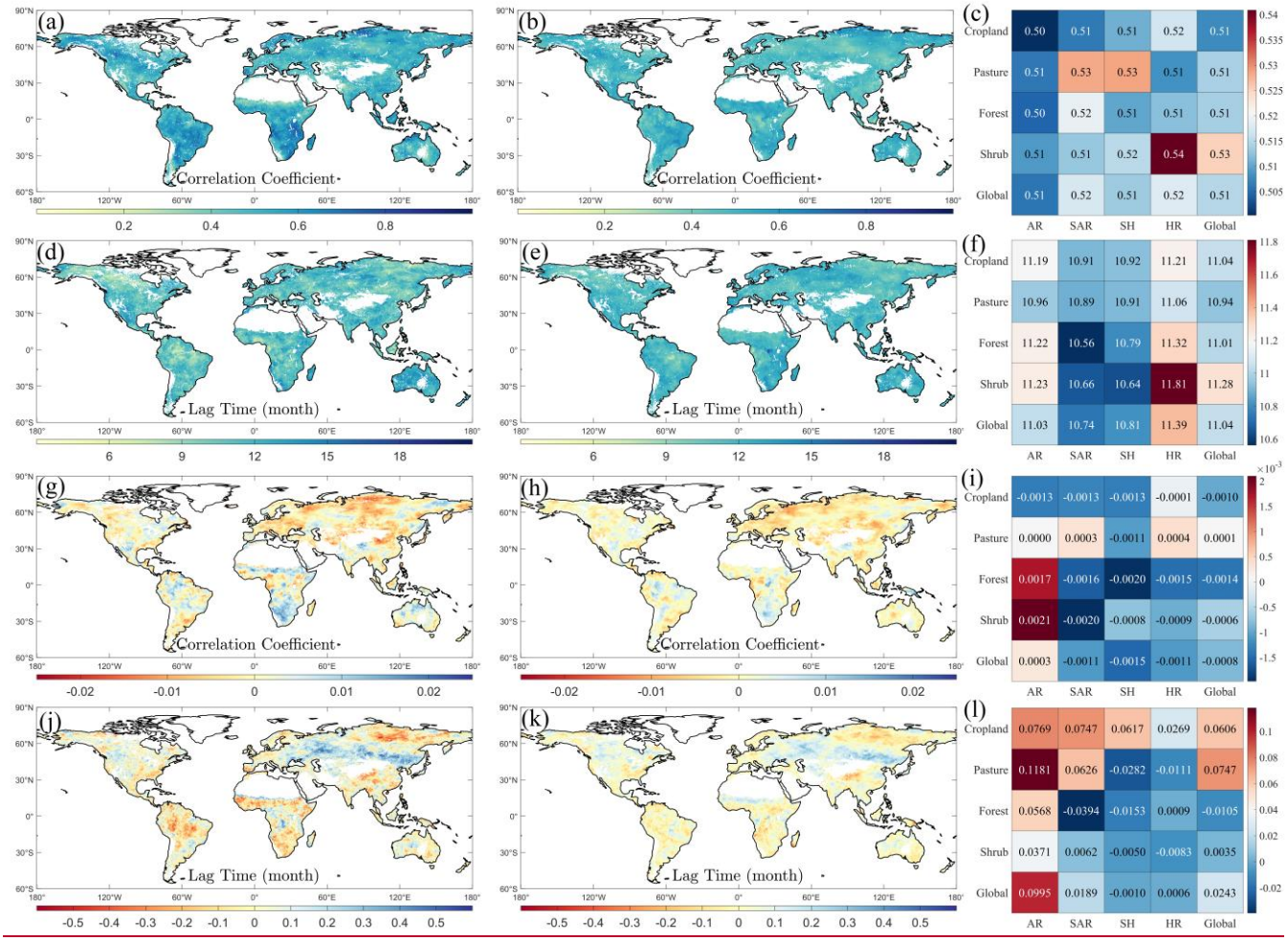

Figure 2. Spatial distribution of the mean and change rates of R_{max} and T_{opt} calculated from ~~(a)~~ the remote sensing observations and ~~(b)~~ the TRENDY multi-model ensemble using an 18-year moving window~~, along with (c) statistical plots for different vegetation types and drought gradients~~. From left to right, the three columns represent remote sensing observations, the TRENDY multi-model ensemble and statistics across different vegetation types and aridity gradients.

4.2. Separation of the Driving Factors of the changes in R_{max} and T_{opt}

Since the spatial distributions simulated by individual DGVM exhibited certain deviations (Figures S9–S11), this study adopted TRENDY multi-model ensemble to separate the effects of CO_2 fertilization, CLI, and LCC on R_{max} and T_{opt}. ~~In addition, similar simulations were conducted using 16-year and 20-year moving windows, which showed high consistency with the results obtained from the 18-year moving window (Figures S12–S13).~~ The results from the TRENDY multi-model ensemble indicated that the negative effect of CO_2 on the R_{max} and the positive effect on T_{opt} were primarily concentrated in the high-latitude regions of the Northern Hemisphere. However, the opposite contributions were observed in the central-southern North America, central and eastern Siberia, as well as southern Central Asia and the Tibetan Plateau~~Mississippi Plain, the Central Siberian Plateau and its eastern mountain ranges, as well as the southern edge of the Mongolian Plateau and the Qinghai-Tibet Plateau~~. In the Southern Hemisphere, CO_2 exerted a predominantly positive effect on the R_{max} and a negative effect on T_{opt},

revealing an overall opposite spatial pattern. In comparison to CO_2, the contributions of CLI and LCC were relatively smaller. The negative contribution of CLI to the R_{max} was mainly distributed in the southern Europe, western Siberia, and the Amazon Basin~~southern part of the East European Plain, the West Siberian Plain, and the Amazon Basin~~, while the negative contribution of LCC was primarily concentrated in the eastern Europe and central-northern Africa~~southern part of the East European Plain and the Chad Basin~~. Both factors showed an overall opposite spatial distribution pattern for their contributions to T_{opt} relative to the R_{max} (Figure 3).

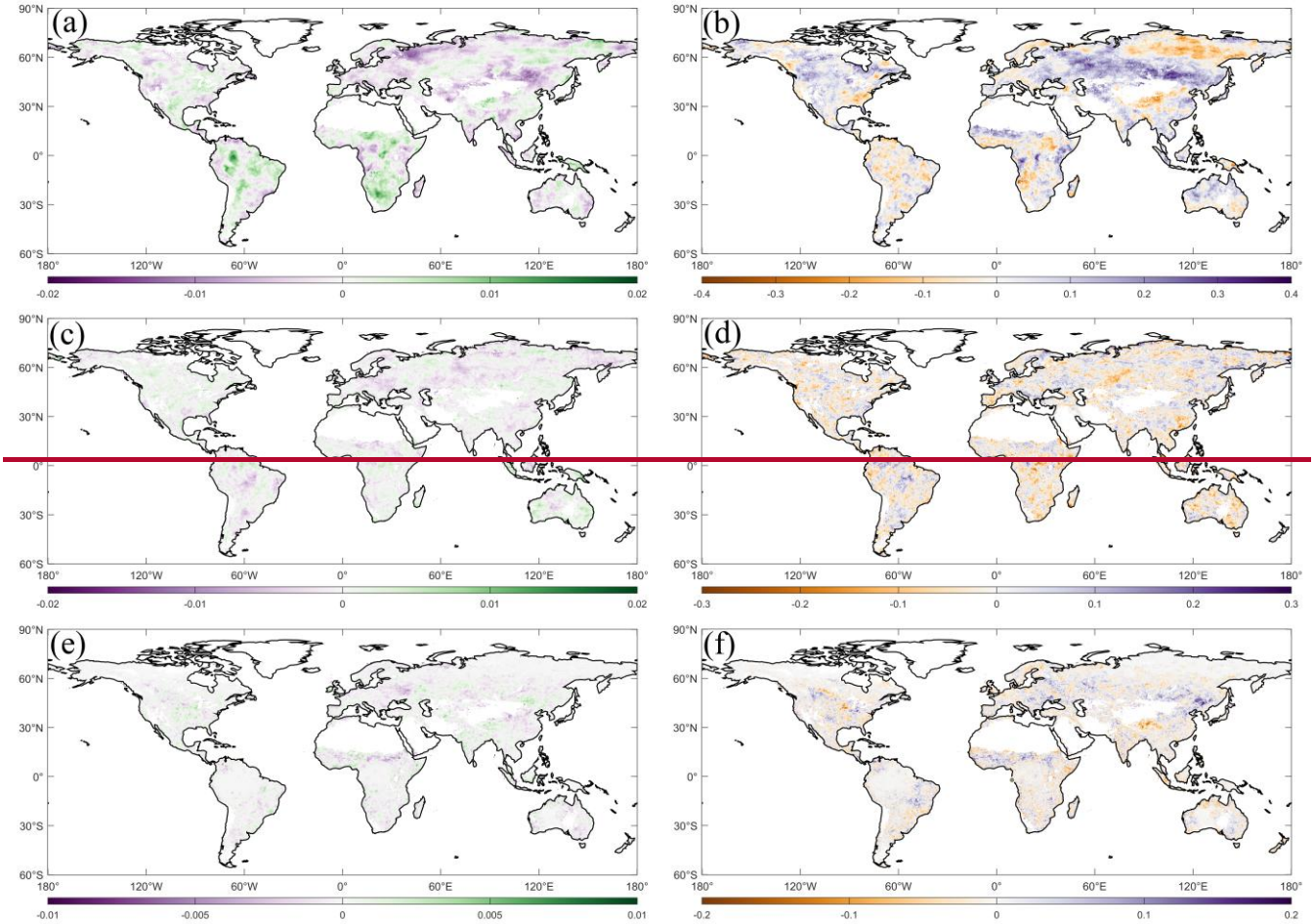
(a)
(b)
(c)
(d)
(e)
(f)
90°N
60°N
30°N
0°
30°S
60°S
180°
120°W
60°W
0°
60°E
120°E
180°
-0.02
-0.01
0
0.01
0.02
-0.4
-0.3
-0.2
-0.1
0.1
0.2
0.3
0.4
-0.005
0.005

359

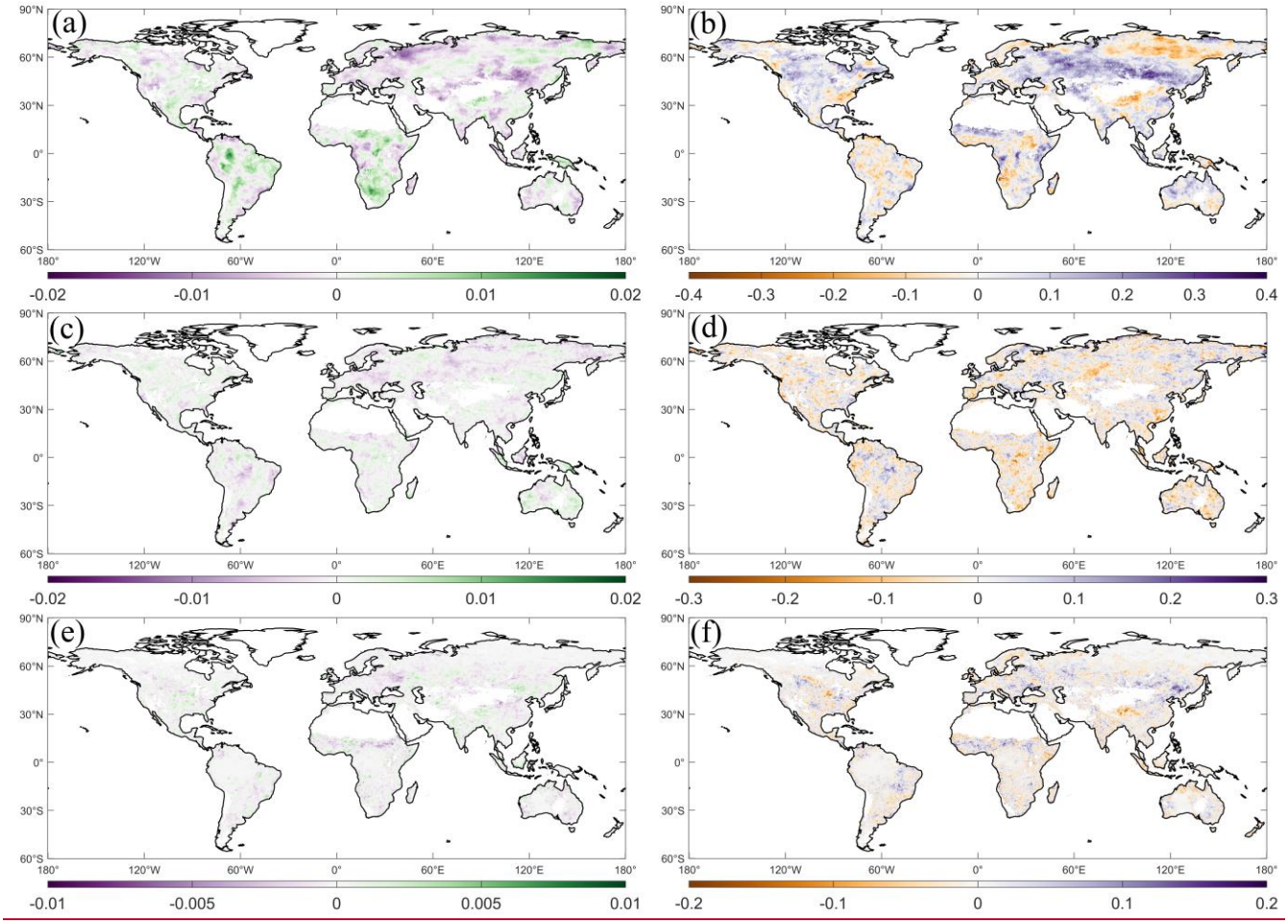

Figure 3. The contributions of CO_2, CLI, and LCC to the R_{max} and T_{opt} under an 18-year moving window. (The left and right columns represented the contributions of variables to the R_{max} and T_{opt}, respectively, with the contributions of CO_2, CLI, and LCC shown from top to bottom.)

At the global scale, the contribution of CO_2 to the R_{max} was approximately -5×10^{-4}/year, while the contributions of LCC and CLI were approximately -0.5×10^{-4}/year and -1.5×10^{-4}/year, respectively. The contributions of CO_2, LCC, and CLI to T_{opt} were 2.3×10^{-2} months/year, 0.2×10^{-2} months/year, and -0.2×10^{-2} months/year, respectively (Figure 4). ~~The observations under the 16-year and 20-year moving window analyses also revealed similar phenomena (Figure S14 – Figure S15).~~ Further analysis across vegetation types and drought gradients revealed that CO_2 generally exerted a negative contribution to R_{max}, with substantial variation among vegetation types. The strongest negative contribution occurred in Cropland, particularly in Cropland within AR (-1.3×10^{-3}/year). Conversely, Forest and Shrub in AR and Pasture in HR exhibited relatively high positive contributions of 0.8×10^{-3}/year, 1.2×10^{-3}/year, and 1.3×10^{-3}/year. In contrast, the contribution of LCC to R_{max} was negligible, with an absolute magnitude less than 0.1×10^{-3}/year. The contribution of CLI to R_{max} was strongly dependent on drought gradients, with its negative effect gradually intensifying from AR to HR. For T_{opt}, the contributions of LCC and CO_2 exhibited broadly consistent patterns across vegetation types and drought gradients. Across drought gradients, the largest contributions of CO_2 and LCC occurred in AR, while across vegetation types, their effects were much greater in cropland and pasture, with

the maximum observed in pastures within AR, where the contributions of CO_2 and LCC reached 0.0815 months/year and 0.0196 months/year, respectively. The contribution of CLI to T_{opt} was predominantly negative in AR and SAR but positive in more humid regions (SH and HR). Specifically, the strongest negative contribution of CLI to T_{opt} occurred in pastures within AR (-0.0196 months/year), whereas the strongest positive contribution was observed in pastures within SH.

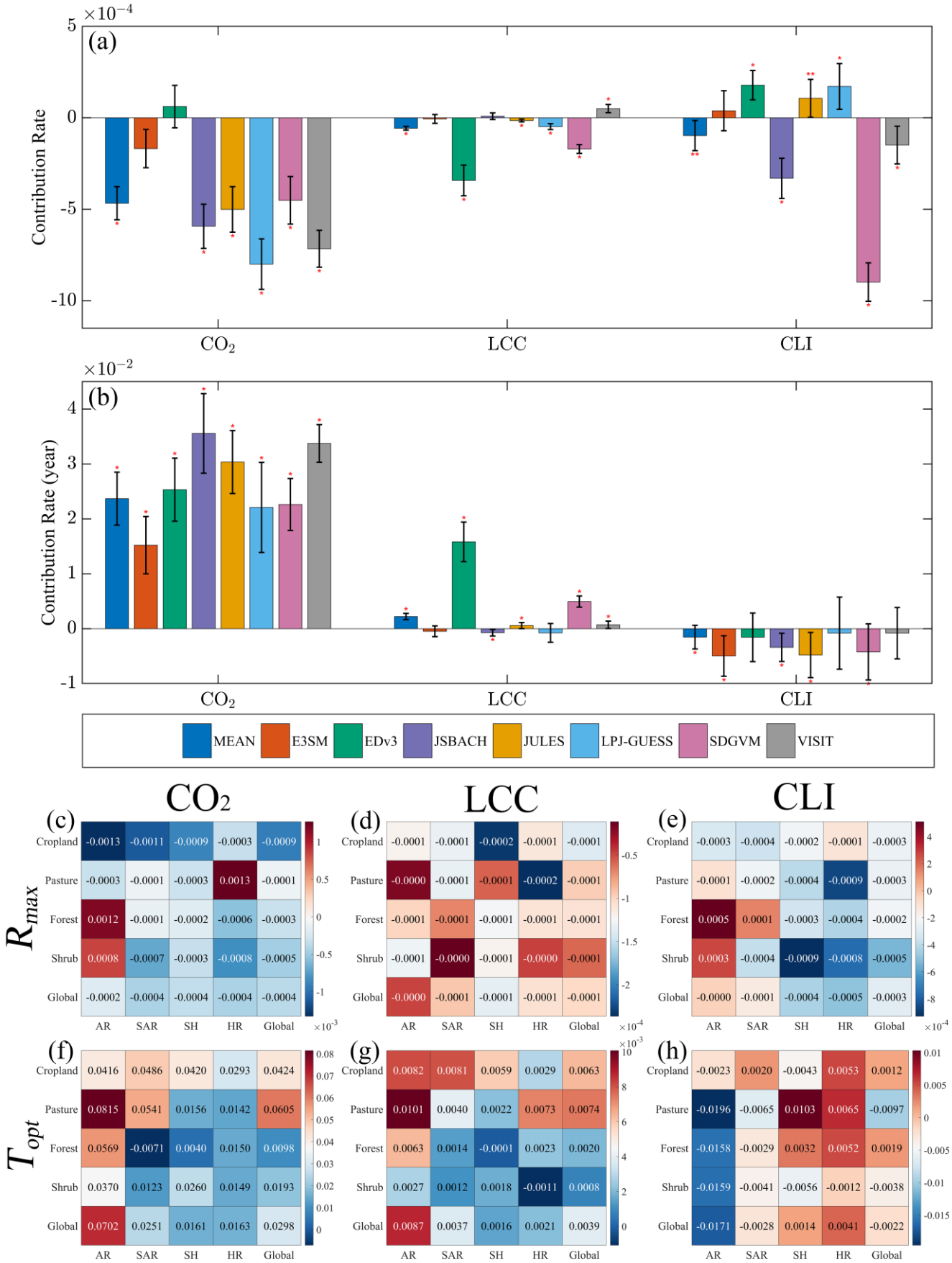

Figure 4. The contributions separated by DGVMs under an 18-year moving window, along with statistical plots for different vegetation types and drought gradients.

Based on the independent contributions of CO_2, LCC and CLI, their spatially dominant regions were further identified (Figure 5). The results indicated that, for both R_{max} and T_{opt}, CO_2 dominated the largest area, followed by CLI, while LCC accounted for the smallest proportion. For R_{max}, the regions dominated by negative CO_2 contributions accounted for 27.3% of the total area and were mainly distributed across the eastern Europe, western Siberia, Central Asia, southeastern South America, central and eastern Africa, and Australia~~East European Plain, West Siberian Plain, Mongolian Plateau, Paraná Plateau, Congo Basin, East African Plateau, and the Australian Great Dividing Range~~. Regions dominated by positive CO_2 contributions covered a slightly smaller proportion (approximately 25.0%), mainly concentrated in the central and eastern Siberia, south-central Africa, and eastern South America~~Central Siberian Plateau and its eastern mountains, the Katanga Plateau, the Karaganda Basin, the Adzhan Plateau, and the Brazilian Highlands and surrounding areas~~. Regions dominated by CLI accounted for 34.5% of the total area and were mainly distributed along the margins of the CO_2-dominated zones, whereas those dominated by LCC accounted for only 13.2%. For T_{opt}, regions dominated by positive CO_2 contributions accounted for 38.2% of the total area and were concentrated between 30°N and 60°N. In contrast, regions dominated by negative CO_2 contributions accounted for 20.2% and were mainly distributed in high-elevation regions such as the eastern Siberia, the Tibetan Plateau, and central-southern North America~~Central Siberian Plateau, Qinghai–Tibet Plateau, and the Mississippi River Plateau~~. The regions dominated by CLI and LCC were relatively scattered. ~~The results derived from the 16-year and 20-year moving window analyses also exhibited a similar distribution pattern (Figure S16 – Figure S17).~~

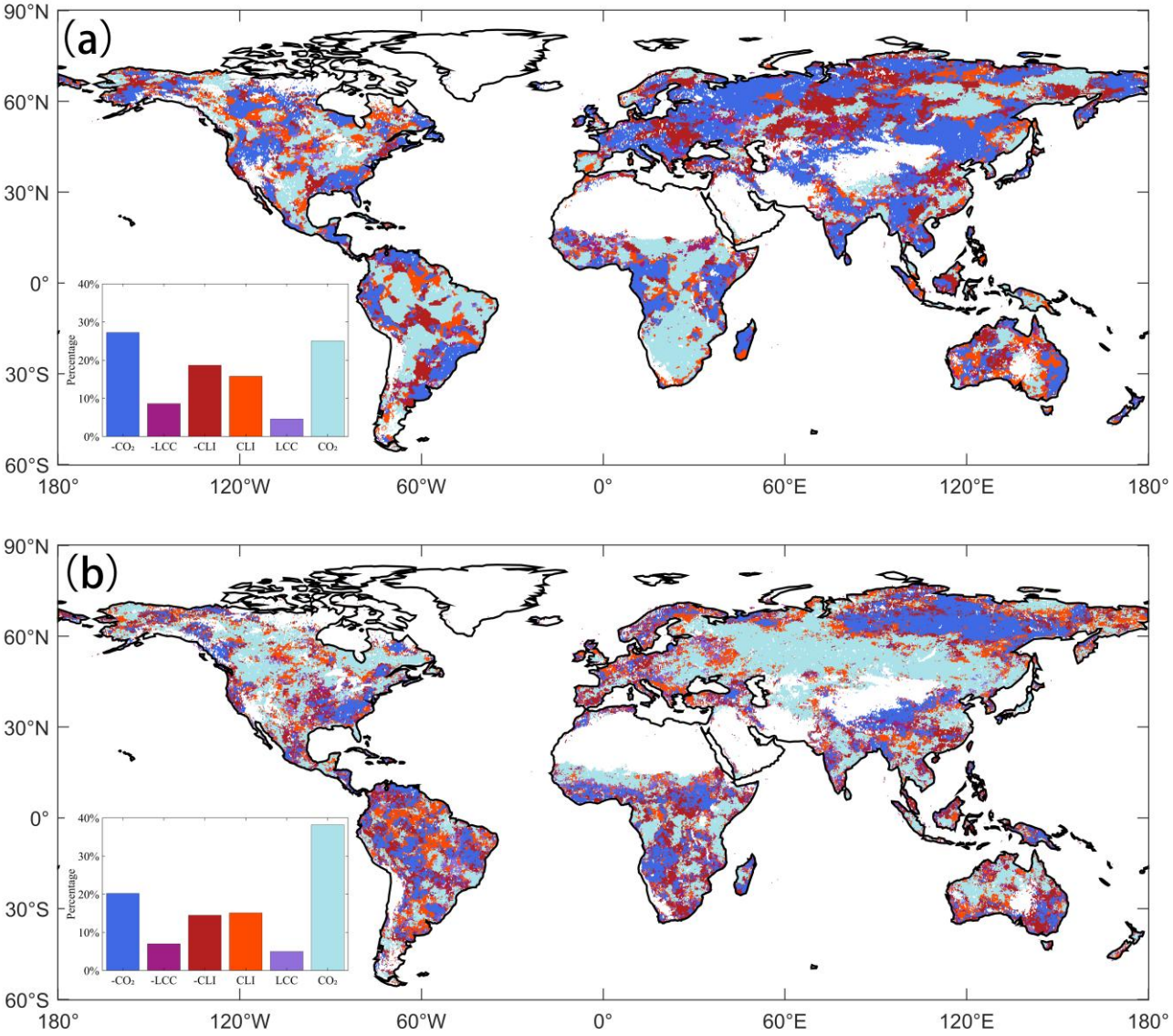

Figure 5. Spatial distribution of the dominant factors of CO_2, LCC, and CLI on (a) the R_{max} and (b) T_{opt} under an 18-year moving window. The bar chart shows the proportions of the dominant areas of CO_2, LCC, and CLI.

4.3. The effects of hydrometeorological ~~hydrothermal~~ factors on the WUE-drought coupled relationship

Using XGBoost and SHAP, we quantified the contributions of hydrometeorological~~hydrothermal~~ factors to the coupling relationship between WUE and drought (Figure 6). From a global perspective, SMsurf was identified as the most important driving factor for both R_{max} and T_{opt}, yet it exhibited nearly opposite influence patterns. Specifically, the effect of SMsurf on R_{max} displayed a unimodal pattern: it reduced R_{max} when SMsurf was below 0.22m^3/m^3, promoted R_{max} between 0.22m^3/m^3 and 0.44m^3/m^3, and peaked around 0.35m^3/m^3. SMsurf showed a significant nonlinear negative relationship with T_{opt}: as SMsurf increased, its effect on T_{opt} shifted from positive to negative at approximately 0.25 m^3/m^3. The effects of SMroot on R_{max} and T_{opt} were opposite to those of SMsurf, although the relative importance of SMroot was lower. Another key driving factor for both R_{max} and T_{opt} was Temp, ranking third and second in relative importance, respectively. Specifically, Temp promoted R_{max}

411 at temperatures below 5.01 °C, inhibited it between 5.01 °C and 18.38 °C with a local minimum near 12 °C, and again exerted
412 a positive effect above 18.38 °C. For T_{opt}, Temp exerted predominantly negative effects below 1.66 °C and above 22.80 °C,
413 while showing positive effects between these thresholds. Other hydrometeorological~~hydrothermal~~ factors also exhibited
414 nonlinear patterns and threshold effects in their influences on R_{max} and T_{opt}.
415

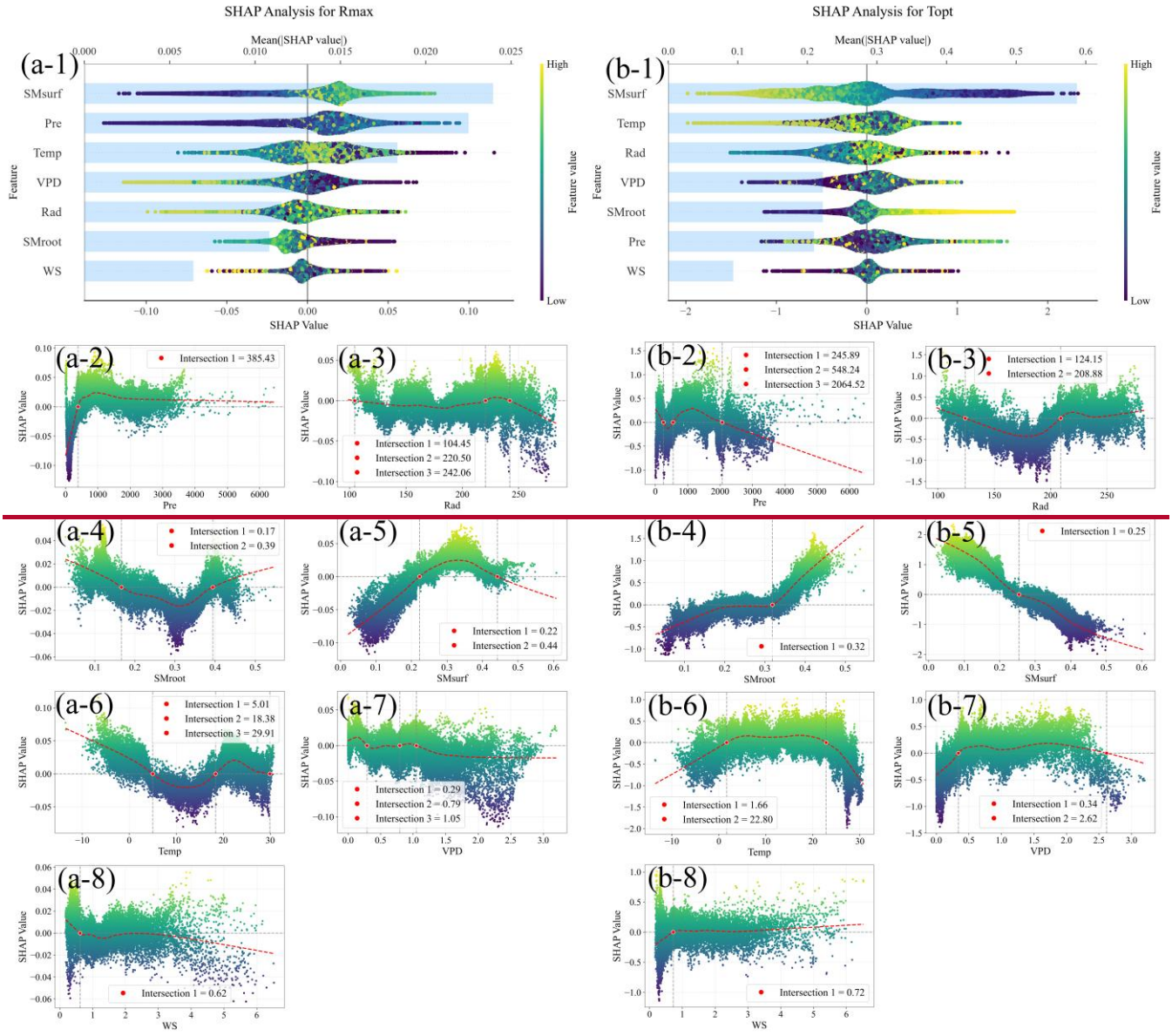

416

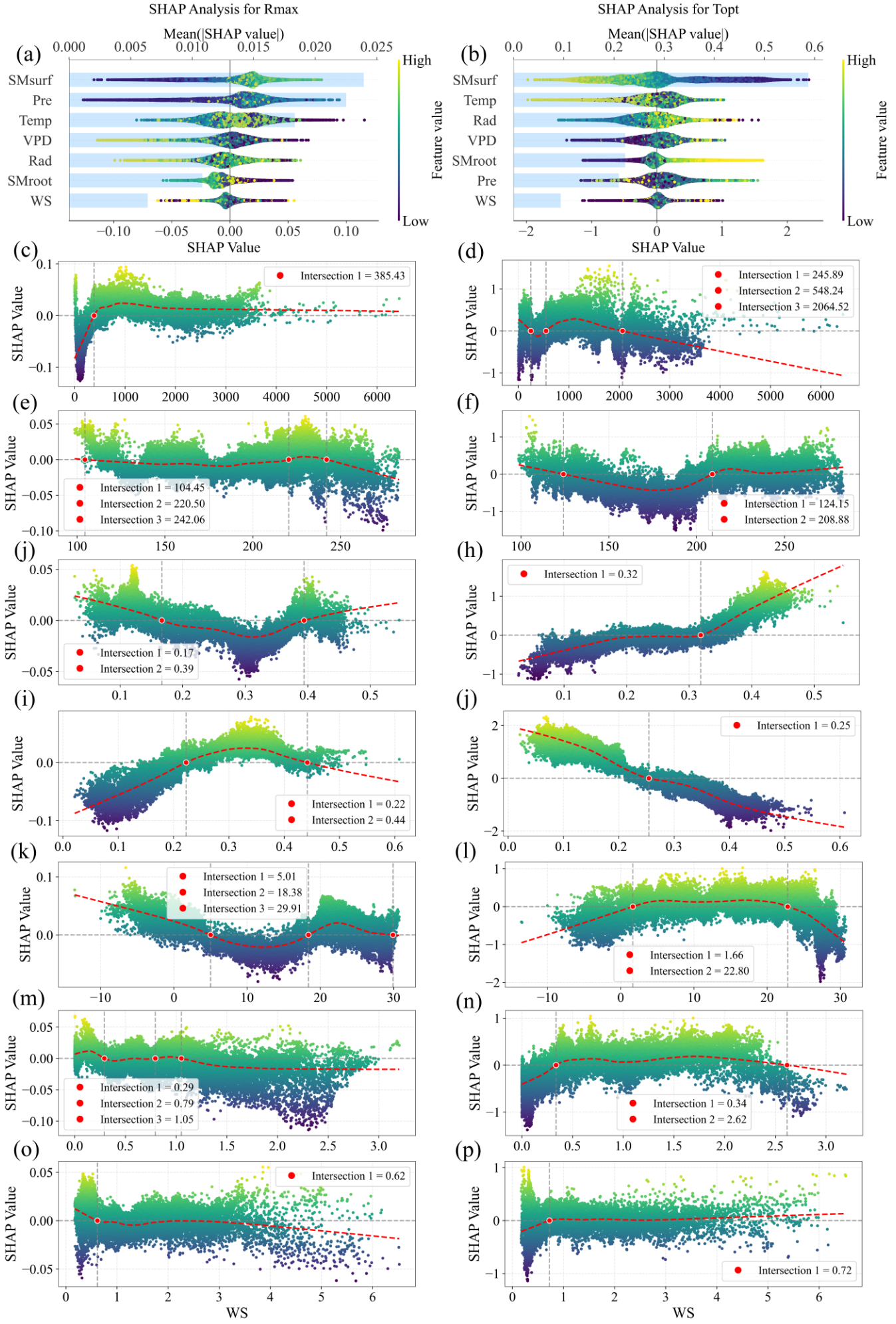
SHAP Analysis for Rmax
SHAP Analysis for Topt
Mean(|SHAP value|)
SMsurf
Pre
Temp
VPD
Rad
SMroot
WS
High
Low
Feature value
SHAP Value
Intersection 1 = 385.43
Intersection 1 = 245.89
Intersection 2 = 548.24
Intersection 3 = 2064.52
Intersection 1 = 104.45
Intersection 2 = 220.50
Intersection 3 = 242.06
Intersection 1 = 124.15
Intersection 2 = 208.88
Intersection 1 = 0.17
Intersection 2 = 0.39
Intersection 1 = 0.32
Intersection 1 = 0.22
Intersection 2 = 0.44
Intersection 1 = 0.25
Intersection 1 = 5.01
Intersection 2 = 18.38
Intersection 3 = 29.91
Intersection 1 = 1.66
Intersection 2 = 22.80
Intersection 1 = 0.29
Intersection 2 = 0.79
Intersection 3 = 1.05
Intersection 1 = 0.34
Intersection 2 = 2.62
Intersection 1 = 0.62
Intersection 1 = 0.72
WS

417

Figure 6. Global and local SHAP analyses of the contributions of hydrothermal factors to (a) R_{max} and (b) T_{opt}. ~~Panels 1 represent the global analysis, while panels 2–9 show the local SHAP analyses for Pre, Rad, SMroot, SMsurf, Temp, VPD and WS on R_{max} and T_{opt}.~~ In the local SHAP analysis, the variables from top to bottom are Pre, Rad, SMroot, SMsurf, Temp, VPD and WS on R_{max} and T_{opt}.

The relative importance rankings and influence mechanisms of hydrothermal factors on R_{max} and T_{opt} varied slightly across vegetation types and drought gradients (Figures S20–S27). In Cropland, VPD was the most important driver of R_{max}, exhibiting a single-threshold effect: VPD exerted a negative influence when exceeding 1.13 hPa and a positive influence when below this threshold. Rad was the dominant driver of T_{opt}, showing two distinct thresholds: Rad promoted T_{opt} below 145.69W/m^2, inhibited it between 145.69 and 204.51W/m^2, and promoted it again above 204.51W/m^2, with a local SHAP maximum at 204.51W/m^2. For Forest, Temp was the most important factor for both R_{max} and T_{opt}. Temp reduced R_{max} between 2.23 °C and 18.65 °C, with the strongest inhibition near 10 °C, whereas it increased T_{opt} between –0.99 °C and 22.00 °C, showing the strongest promotion around 10 °C. For Pasture, Pre and SMsurf were the most critical factors influencing R_{max} and T_{opt}, respectively. Pre decreased R_{max} when below 438.46 mm but increased it above this value, while SMsurf promoted T_{opt} below 0.24 m^3/m^3 and inhibited it above. For Shrub, SMsurf was the most important driver for both R_{max} and T_{opt} with thresholds of 0.23 m^3/m^3 and 0.20 m^3/m^3, respectively, showing opposite effects across the thresholds.

Across drought gradients, Pre and SMsurf were the most important drivers of R_{max} and T_{opt}, respectively, in AR. The effect of Pre on R_{max} shifted from negative to positive at 245.03 mm, while that of SMsurf on T_{opt} changed from positive to negative at 0.12m^3/m^3. In SAR, Temp and Rad were the most critical drivers of R_{max} and T_{opt}, respectively. The influence of Temp on R_{max} exhibited pronounced nonlinearity: Temp decreased R_{max} below 16.91 °C (with a local minimum near 13 °C) but promoted T_{opt} above 16.91 °C, showing a local maximum near 23 °C. Rad inhibited T_{opt} below 206.65 W/m^2 but promoted it above this threshold. In SH, VPD and Rad were the dominant drivers of R_{max} and T_{opt}, respectively; VPD increased R_{max} when exceeding 0.58 hPa, while lower VPD values reduced it, and the positive effects of Rad on T_{opt} were concentrated between 598.44 and 1472.70 W/m^2. In HR, Temp was the most critical driver for both R_{max} and T_{opt}, with their partial dependence plots exhibiting nearly opposite patterns.

The results derived from PCMCI+ revealed a complex causal network between hydrothermal factors, R_{max}, and T_{opt} (Figure 7). At the global scale, WS exhibited a negative causal relationship with R_{max}, while R_{max}, in turn, negatively influenced Pre, Rad, and Temp. Although many factors did not exert a direct causal effect on R_{max}, they influenced it indirectly through various pathways. For instance, VPD affected R_{max} indirectly via WS, while Rad influenced Temp, which subsequently impacted WS and ultimately affected R_{max}. For T_{opt}, Rad and WS exhibited direct negative and positive causal relationships,

447 respectively. Conversely, T_{opt} exerted a direct positive causal effect on Pre and a direct negative effect on Temp. Additionally,
448 SMroot and SMsurf were causally linked to T_{opt}, though the direction of their influence remained unclear.

449 To further explore the causal network under different vegetation types and drought gradients, we conducted an in-depth
450 statistical analysis, examining interactions within overlapping regions of vegetation type and drought gradient (Figure S28–
451 Figure S31). In terms of drought gradients, the causal network structures in AR and SAR were relatively simple. In AR, R_{max}
452 was directly influenced by Rad, while T_{opt} showed little causal linkage with other hydrothermal factors. In SAR, R_{max} was not
453 directly affected by hydrothermal factors but exhibited direct causal relationships with VPD and WS. Meanwhile, T_{opt} was
454 positively influenced by Temp and Pre, negatively influenced by WS, and had an undefined negative causal relationship with
455 SMsurf. Conversely, the causal relationships in SH and HR were considerably more intricate. Beyond the complex interactions
456 among hydrothermal factors and their indirect effects on R_{max} and T_{opt}, hydrothermal factors also directly influenced R_{max} and
457 T_{opt} through multiple pathways. For example, in SH, both Pre and Rad exerted direct negative causal effects on R_{max}, while
458 Temp had a direct positive influence. From the perspective of vegetation types, the causal networks in Cropland, Pasture, and
459 Forest were relatively complex, whereas Shrub exhibited a simpler structure. In Cropland, R_{max} was directly and negatively
460 influenced by Rad, while T_{opt} was directly and positively affected by Rad but negatively impacted by SMroot and WS. In
461 Pasture, R_{max} was negatively influenced by Pre, while T_{opt} was negatively affected by SMroot. In Forest, R_{max} was negatively
462 influenced by Rad, whereas T_{opt} was negatively influenced by VPD and WS but positively affected by Pre and Temp. In Shrub,
463 SMroot exerted a direct negative influence on R_{max}, while Temp had a direct positive effect. T_{opt}, on the other hand, was mainly
464 influenced by Pre through a direct positive causal relationship and was negatively influenced by SMsurf and Temp.

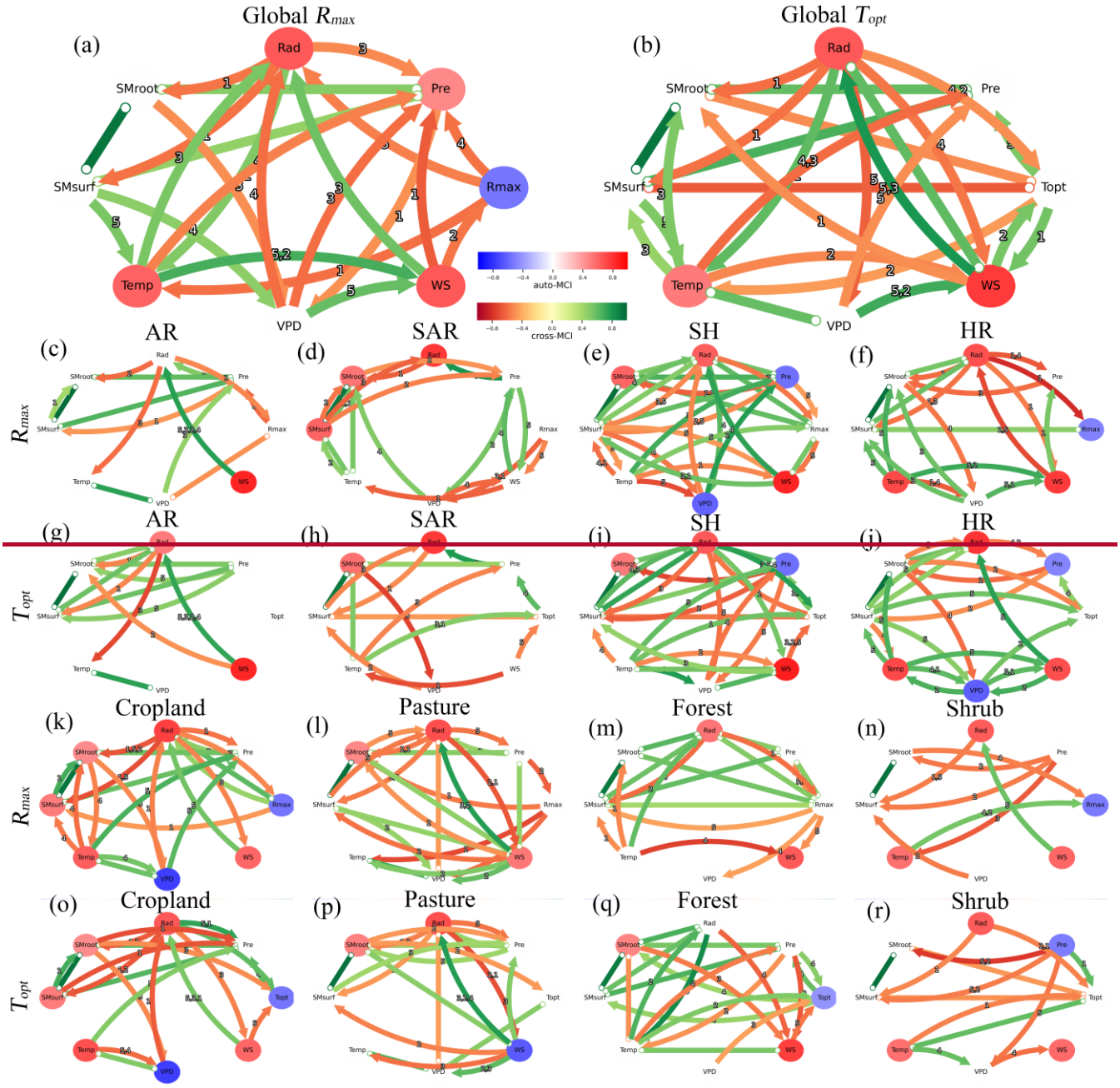
Global R_{max}
Global T_{opt}
(a)
(b)
Rad
SMroot
Pre
SMsurf
Rmax
Temp
WS
VPD
Topt
auto-MCI
cross-MCI
AR
SAR
SH
HR
(c)
(d)
(e)
(f)
(g)
(h)
(i)
(j)
R_{max}
T_{opt}
Cropland
Pasture
Forest
Shrub
(k)
(l)
(m)
(n)
(o)
(p)
(q)
(r)

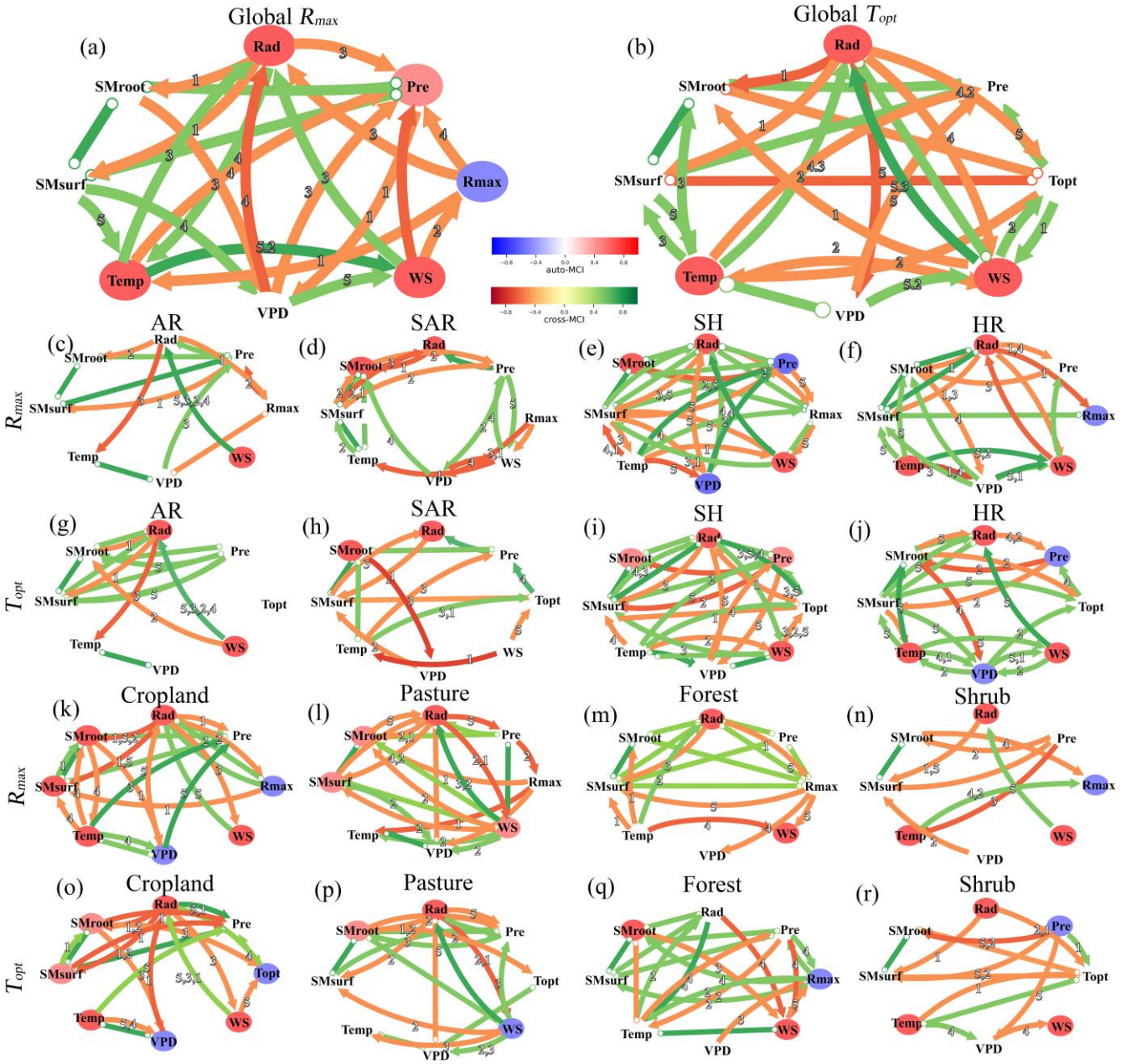

Figure 7. Causal network diagram of hydrothermal factors, R_{max}, and T_{opt} across different vegetation types, drought gradients, and the global scale.

5. Discussion

5.1 Robustness of the results

To ensure the robustness of the remotely sensed WUE observations, we averaged three sets of GPP and ET products and validated the results against data from 85 FLUXNET 2015 sites (Figure S1, Table S1). The results indicated a high consistency between the multi-product average WUE from remote sensing and the site data (R = 0.62, Figure S2). To confirm the alignment of the selected DGVMs with the remote sensing observations, we performed calculations for all models within TRENDY v12 and identified seven models whose trends under the S3 scenarios were consistent with the remote sensing observations. As

shown in the Taylor diagram, the multi-model ensemble results exhibited high correlation with the remote sensing observations and lower standard deviation, supporting the credibility of the separated contributions of CO_2, LCC, and CLI (Figure S6). To mitigate the impact of interannual variations on trend significance, all calculations were performed within an 18-year moving window. To test the robustness of the R_{max} and T_{opt} under different window choices, we repeated all calculations using 16-year and 20-year windows, which yielded similar conclusions (Figure S7-Figure S17). Therefore, we considered our results to be highly reliable.

5.2 Spatiotemporal variation characteristics of the coupling relationship

This study pioneers the identification of optimal time scale for WUE response to drought coupling, demonstrating significant spatiotemporal heterogeneity. Temporally, the optimal WUE-drought response scale exhibited an upward trend (Figure 1), indicating a delayed WUE response to drought and, consequently, an enhanced buffering capacity of vegetation against drought has been enhanced (Peters et al., 2018; Frank et al., 2015). This phenomenon likely stems from climate change-driven drought intensification, compelling vegetation to utilize slow-response water sources like deep soil moisture or groundwater (Miguez-Macho and Fan, 2012). However, Tang et al. (2024) employed GPP as a proxy for vegetation and found that vegetation sensitivity to drought increased and its response time shortened, which appears to contradict our findings. However, that study focused only on single indicators such as GPP, which reflect vegetation photosynthesis, whereas WUE likely plays a more complex role in regulating water and carbon dynamics. ~~Li et al. (2025) found, from the perspective of drought propagation, that stomata play a crucial role in regulating water use efficiency to resist drought. Therefore, it is reasonable to infer that under drought stress, stomatal behavior primarily buffers drought impacts by regulating evapotranspiration.~~ In addition, differences in the definition of sensitivity, data sources, methods, research periods, and research areas might lead to different conclusions. Different types of droughts might also result in different outcomes. Therefore, our findings did not necessarily refute previous views. However, we firmly believe that considering the time scale in the response of WUE to drought is a crucial step in revealing the dynamic relationship between WUE and SPEI.

Across drought gradients, the optimal ~~time~~ drought scale ~~for WUE and SPEI~~ in arid regions was significantly shorter than in humid regions. This phenomenon could be explained by the resource limitation hypothesis (Huxman et al., 2004) , which posited that in humid regions, plant growth was generally limited by light or nutrient availability, whereas in arid regions, it was primarily constrained by water scarcity (Maurer et al., 2020; Knapp et al., 2024). Larger T_{opt} were mainly concentrated in humid, energy-limited regions, where drought conditions caused by insufficient precipitation were often accompanied by high temperatures and intense solar radiation, thereby enhancing the resistance of WUE to drought (Gentine et al., 2019; Walther et al., 2019). For instance, Miller et al. (2023) reported a sustained increase in plant photosynthesis during spring droughts

across most vegetated areas of the Northern Hemisphere. Similarly, during recent drought events such as those in Europe in 2018 and 2022, several energy-limited ecosystems also exhibited enhanced plant activity (Bastos et al., 2020). Differences in vegetation adaptation strategies along drought gradients might also have led to distinct response times. Vegetation in arid regions optimized water use through stomatal dynamics, whereas humid ecosystems buffered drought effects via deep rooting systems and canopy shading (Klein et al., 2011). A shorter response time might indirectly indicate higher sensitivity (Vicente-Serrano et al., 2013); thus, our findings also supported previous conclusions that vegetation in arid regions exhibited stronger drought sensitivity (De Keersmaecker et al., 2015; Seddon et al., 2016). However, we found that this pattern was shifting between arid and humid regions. Specifically, the optimal drought ~~time~~ scale ~~for WUE and SPEI~~ in arid regions showed the most rapid increase, whereas the rate of change in humid regions was much smaller or even declined. We attributed this discrepancy in the consideration of time scales.

From the perspective of vegetation types, the optimal drought scale~~response time of WUE to drought~~ increased rapidly in Cropland and Pasture, increased slightly in Shrub, but decreased in Forest. This pattern might result from the stronger influence of human activities on Cropland and Pasture, where irrigation and fertilization altered the water and nutrient conditions of these ecosystems (Jaramillo et al., 2018). On the one hand, irrigation maintained adequate soil moisture at all times. On the other hand, sufficient nitrogen supply ensured high photosynthetic nitrogen-use efficiency in crop leaves, indicating that even under partial stomatal closure and limited intercellular CO_2 concentration, leaves were still able to efficiently utilize the available CO_2 for photosynthesis. In contrast, Shrub and Forest were mostly subject to natural conditions. The slight increase in T_{opt} observed in Shrub might have reflected their conservative, isohydric water-use strategy (Yang et al., 2016). The decrease in T_{opt} in Forest might have been attributed to continued transpiration under water stress, which persisted due to their extensive canopies and residual hydraulic function, thereby shortening the response time to drought (Novick et al., 2016). These findings collectively reveal vegetation-drought coupling as a nonlinear outcome of climate forcing, ecological adaptation, and anthropogenic intervention, necessitating multi-scale models and sustained monitoring to unravel critical thresholds (Reichstein et al., 2013).

5.3. Influencing factors of coupling relationship

TRENDY multi-model simulations identified CO_2 fertilization as the dominant driver weakening WUE-SPEI coupling, as evidenced by a decrease in the maximum correlation coefficient and an increase in the optimal drought timescale (Figure 4). On the one hand, elevated atmospheric CO_2 enhances the carboxylation efficiency of Rubisco, thereby directly promoting GPP and enabling vegetation to maintain relatively high carbon assimilation without increased water supply; consequently, the synchrony between decreases in GPP and SPEI is weakened. On the other hand, elevated atmospheric CO_2 induces partial

stomatal closure, thereby reducing transpiration water loss (Keenan et al., 2013). These mechanisms play a critical role in preventing rapid declines in WUE under drought conditions, thereby directly reducing its sensitivity to meteorological drought. Moreover, the CO_2 fertilization effect promotes deeper root distribution and adaptive changes in hydraulic traits, leading plants to increasingly rely on water stored from past precipitation in deeper unsaturated soil layers or groundwater to maintain carbon-water balance under drought stress (Zhang et al., 2026). This enhances the ecohydrological buffering capacity of vegetation against short-term meteorological drought, as reflected by an increase in the optimal drought timescale. Theoretically, these processes occur at the leaf scale, enhancing intrinsic water use efficiency (Li et al., 2025), however, cross-scale dependencies allow these effects to propagate to the ecosystem scale. ~~Elevated CO_2 enhanced WUE directly through stimulated photosynthesis and reduced stomatal conductance (Keenan et al., 2013) , thereby strengthening the resistance of WUE to drought.~~ Land-use changes exert secondary but critical impacts, including tropical deforestation, forest degradation, and afforestation programs, all of which gradually altered global vegetation patterns. In addition, agricultural management practices such as irrigation, fertilization, and crop modification did not change vegetation cover types but still influenced vegetation adaptability to environmental conditions. Chen et al. (2019) found that human land-use practices might have contributed to more than one-third of the global vegetation increase, particularly in extensive cropland regions—most notably in China (25%) and India (6.8%). Therefore, we reasonably inferred that LCC driven by human interventions enhanced ecosystem resilience to drought and other extreme events, particularly in croplands. This was manifested in our results as LCC contributed a negative effect in R_{max} and a positive effect in T_{opt}.

Although TRENDY multi-model simulations indicated that the influence of climate change was minimal, this study employed XGBoost and SHAP to reveal how meteorological factors affected the WUE–SPEI coupling relationship. SMsurf was identified as the most important driving factor, exhibiting nearly opposite effects on R_{max} and T_{opt} and a significant threshold response (Figure 6). In fact, this remained closely associated with increased atmospheric CO_2. Previous studies suggested that although elevated atmospheric CO_2 could reduce plant water loss by decreasing stomatal conductance—thereby theoretically slowing soil moisture depletion (Gray et al., 2016) —the elevated CO_2 was accompanied by increased leaf temperature and accelerated evaporation from shallow soils, which offset this water-saving effect (Wilson et al., 1999), ultimately promoting soil moisture depletion(Kellner et al., 2019). As the direct “water reservoir” for vegetation, surface soil moisture limited plant water supply and reduced photosynthesis, thereby exerting a profound influence on the WUE–SPEI coupling relationship (Liu et al., 2020; Martínez-Vilalta et al., 2014). Along the drought gradient, precipitation was the most important factor influencing the WUE–SPEI coupling in arid regions, with SMsurf ranking third in importance. In contrast, in humid regions, temperature and radiation were the dominant factors, while SMsurf ranked fifth and sixth in importance for R_{max} and T_{opt}, respectively (Figure S23; Figure S26), consistent with previous findings. Vegetation in arid regions was typically

water-limited, and precipitation, as its direct water source, played a crucial regulatory role in drought response (Li et al., 2022b). In contrast, in humid regions with sufficient water supply, vegetation responses to drought were primarily controlled by energy-related factors such as temperature and radiation(Liu et al., 2025). Across vegetation types, the dominant factors influencing the WUE–SPEI coupling were more clearly defined in Forest and Shrub, being temperature and surface soil moisture, respectively, which were closely related to their rooting patterns and drought-resistance strategies (Yang et al., 2025). In contrast, the dominant factors in Pasture and Cropland were more complex, likely resulting from vegetation structural diversity and intensive human interventions(Liu et al., 2018).

5.4. Limitations and future prospects

This study provides valuable insights into the dynamic coupling between WUE and meteorological drought; however, several limitations remain. Among various drought types, meteorological drought is the most prevalent, which is why SPEI was selected in this study (Zhou et al., 2024). Previous studies have demonstrated that other drought types are closely linked to meteorological drought, often triggered by precipitation anomalies and exhibiting certain lag effects; in contrast, heatwaves typically precede meteorological drought, indicating that heatwave-drought events evolve dynamically through a sequential triggering process (Yan et al., 2025a). Different drought types operate through distinct mechanisms and exert varying impacts on WUE. Furthermore, this study focuses solely on WUE at the ecosystem scale, while the coupling relationships between drought and WUE at the leaf and canopy scales remain unclear (Wang et al., 2026b). Therefore, future studies should further investigate the dynamic coupling between WUE across multiple scales and different types of heatwaves and droughts, as WUE at different scales responds differently across various stages of heatwave-drought propagation. Such efforts will facilitate a more comprehensive understanding of vegetation responses to drought and provide a stronger theoretical foundation for evaluating carbon-water cycles under climate change.

6. Conclusion

Understanding the coupling relationship between WUE and drought is crucial for assessing the impact of drought on terrestrial ecosystem carbon-water cycles. To this end, we investigated the spatiotemporal patterns of the WUE-SPEI coupling relationship from 1982 to 2018 globally. Using the DGVMs, we separated the contributions of CO_2 fertilization, CLI, and LCC to the changes in WUE-drought coupling relationship. Furthermore, the XGBoost combined with SHAP and PCMCI+ were employed to elucidate the mechanisms and influencing pathways of hydrothermal factors on the coupling relationship. Our key findings included the following:

(1) R_{max} decreased at a rate of -0.0003/year, while T_{opt} increased at a rate of 0.0155 months/year, indicating the buffer capacity of WUE against drought was enhanced. The rates of change in R_{max} and T_{opt} varied substantially across drought gradients and vegetation types. R_{max} increased most rapidly in Shrub within AR at 0.0021/year, whereas the largest decreases occurred in Shrub within SAR and Forest within SH, both at -0.0020/year. T_{opt} increased most rapidly in Pasture within AR at 0.1181 months/year, while it decreased most markedly in Forest within SAR at -0.0394 months/year.

(2) CO_2 fertilization was identified as the primary cause for the weakening of the coupling relationship. SMsurf was identified as the most critical driver, exhibiting nearly opposite effects and significant threshold effects on R_{max} and T_{opt}.

(3) At the global scale, WS exhibited a direct negative causal relationship with R_{max}, while Rad and WS had direct negative and positive causal effects on T_{opt}, respectively. The complex causal networks under different vegetation types and drought gradients were also revealed.

Overall, our findings highlighted an enhanced resistance of WUE to drought, manifested as a reduced correlation and a delayed response time. Moreover, vegetation under different drought gradients gradually adjusted its water-use strategies to maintain WUE stability. These findings encourage a reassessment of the WUE–drought relationship, offering new insights to support the sustainable development of ecosystems under climate change.

Author Contribution declaration

Conceptualization and supervision: Z.W. and Y.L.; Design and methodology: Z.W., R.W., and Y.L.; Data analysis: Z.W., R.W., S.S., Z.Y., and W.Y.; Data curation: Z.W., Z.W., and H.S.; Writing-original draft preparation: Z.W. and Y.L.; Writing-review and editing: S.S. and W.Y..

Declaration of Competing Interest

The authors declare that they have no known competing financial interests or personal relationships that could have appeared to influence the work reported in this paper.

Code/Data availability

The datasets that support the findings of this study are publicly available. The GLASS GPP dataset is available at http://glass.umd.edu/Download.html. The FluxCom Gpp dataset is available at http://fluxcom.org/CF-Download/. The NIRv Gpp dataset is at https://data.tpdc.ac.cn/zh-hans/data/d6dff40f-5dbd-4f2d-ac96-55827ab93cc5. The ERA5-Land ET dataset is available at https://cds.climate.copernicus.eu/datasets/reanalysis-era5-pressure-levels-monthly-means?tab=overview. The GLASS ET dataset is available at http://glass.umd.edu/Download.html. The GLEAM ET is available at https://www.gleam.eu.CRU ts4.07 is available at https://crudata.uea.ac.uk/cru/data/hrg/cru_ts_4.07/. Collection of CRU JRA forcing datasets of gridded land surface blend of Climatic Research Unit (CRU) and Japanese reanalysis (JRA) data (CRU JAR) is available at https://data-search.nerc.ac.uk/geonetwork/srv/api/records/863a47a6d8414b6982e1396c69a9efe8. The

HIstoric Land Dynamics Assessment+ (HILDA+) is available at https://doi.pangaea.de/10.1594/PANGAEA.921846?format=html#download. Global Aridity Index and Potential Evapotranspiration (ET0) Database: Version 3 is available at https://figshare.com/articles/dataset/Global_Aridity_Index_and_Potential_Evapotranspiration_ET0_Climate_Database_v2/7504448/5; FLUXNET2015 Dataset is available at https://fluxnet.org/data/fluxnet2015-dataset/. Simulations from TRENDY land surface models are available on request to S.S. (s.a.sitch@exeter.ac.uk) and P.F. (p.friedlingstein@exeter.ac.uk). Code will be made available on request.

Funding

This work was supported by National Natural Science Foundation of China (No. 42477522); the Science and Technology Plan Project of the Tibet Autonomous Region (No. XZ202501ZY0045); the Inner Mongolia Autonomous Region Science and Technology Plan (No. 2025YFHH0224); the Shanxi Key Laboratory of Earth Surface Processes and Resource Ecology Security in Fenhe River Basin (No. FHKF202402).

Acknowledgments

We acknowledge for the data support from 'Loess plateau science data center, National Earth System Science Data Sharing Infrastructure, National Science & Technology Infrastructure of China, National Tibetan Plateau Scientific Data Center'.

Reference

Bastos, A., Ciais, P., Friedlingstein, P., Sitch, S., Pongratz, J., Fan, L., Wigneron, J. P., Weber, U., Reichstein, M., Fu, Z., Anthoni, P., Arneth, A., Haverd, V., Jain, A. K., Joetzjer, E., Knauer, J., Lienert, S., Loughran, T., McGuire, P. C., Tian, H., Viovy, N., and Zaehle, S.: Direct and seasonal legacy effects of the 2018 heat wave and drought on European ecosystem productivity, Science Advances, 6, eaba2724, doi:10.1126/sciadv.aba2724, 2020.

Beer, C., Ciais, P., Reichstein, M., Baldocchi, D., Law, B. E., Papale, D., Soussana, J.-F., Ammann, C., Buchmann, N., Frank, D., Gianelle, D., Janssens, I. A., Knohl, A., Köstner, B., Moors, E., Roupsard, O., Verbeeck, H., Vesala, T., Williams, C. A., and Wohlfahrt, G.: Temporal and among-site variability of inherent water use efficiency at the ecosystem level, Global Biogeochemical Cycles, 23, https://doi.org/10.1029/2008GB003233, 2009.

Beguería, S., Vicente-Serrano, S. M., Reig, F., and Latorre, B.: Standardized precipitation evapotranspiration index (SPEI) revisited: parameter fitting, evapotranspiration models, tools, datasets and drought monitoring, International Journal of Climatology, 34, 3001-3023, 10.1002/joc.3887, 2014.

Boulton, C. A., Lenton, T. M., and Boers, N.: Pronounced loss of Amazon rainforest resilience since the early 2000s, Nature Climate Change, 12, 271-278, 10.1038/s41558-022-01287-8, 2022.

Chen, C., Park, T., Wang, X., Piao, S., Xu, B., Chaturvedi, R. K., Fuchs, R., Brovkin, V., Ciais, P., Fensholt, R., Tømmervik, H., Bala, G., Zhu, Z., Nemani, R. R., and Myneni, R. B.: China and India lead in greening of the world through land-use management, Nature Sustainability, 2, 122-129, 10.1038/s41893-019-0220-7, 2019.

Chen, T., Wang, Y., and Peng, L.: Advanced time-lagged effects of drought on global vegetation growth and its social risk in the 21st century, Journal of Environmental Management, 347, 119253, https://doi.org/10.1016/j.jenvman.2023.119253, 2023.

De Keersmaecker, W., Lhermitte, S., Tits, L., Honnay, O., Somers, B., and Coppin, P.: A model quantifying global vegetation resistance and resilience to short-term climate anomalies and their relationship with vegetation cover, Global Ecology and Biogeography, 24, 539-548, https://doi.org/10.1111/geb.12279, 2015.

Frank, D. C., Poulter, B., Saurer, M., Esper, J., Huntingford, C., Helle, G., Treydte, K., Zimmermann, N. E., Schleser, G. H., Ahlström, A., Ciais, P., Friedlingstein, P., Levis, S., Lomas, M., Sitch, S., Viovy, N., Andreu-Hayles, L., Bednarz, Z., Berninger, F., Boettger, T., D'Alessandro, C. M., Daux, V., Filot, M., Grabner, M., Gutierrez, E., Haupt, M., Hilasvuori, E., Jungner, H., Kalela-Brundin, M., Krapiec, M., Leuenberger, M., Loader, N. J., Marah, H., Masson-Delmotte, V., Pazdur, A., Pawelczyk, S., Pierre, M., Planells, O., Pukiene, R., Reynolds-Henne, C. E., Rinne, K. T., Saracino, A., Sonninen, E., Stievenard, M., Switsur, V. R., Szczepanek, M., Szychowska-Krapiec, E., Todaro, L., Waterhouse, J. S., and Weigl, M.: Water-use efficiency and transpiration across European forests during the Anthropocene, Nature Climate Change, 5, 579-583, 10.1038/nclimate2614, 2015.

Friedlingstein, P., O'Sullivan, M., Jones, M. W., Andrew, R. M., Bakker, D. C. E., Hauck, J., Landschützer, P., Le Quéré, C., Luijkx, I. T., Peters, G. P., Peters, W., Pongratz, J., Schwingshackl, C., Sitch, S., Canadell, J. G., Ciais, P., Jackson, R. B., Alin, S. R., Anthoni, P., Barbero, L., Bates, N. R., Becker, M., Bellouin, N., Decharme, B., Bopp, L., Brasika, I. B. M., Cadule, P., Chamberlain, M. A., Chandra, N., Chau, T. T. T., Chevallier, F., Chini, L. P., Cronin, M., Dou, X., Enyo, K., Evans, W., Falk, S., Feely, R. A., Feng, L., Ford, D. J., Gasser, T., Ghattas, J., Gkritzalis, T., Grassi, G., Gregor, L., Gruber, N., Gürses, Ö., Harris, I., Hefner, M., Heinke, J., Houghton, R. A., Hurtt, G. C., Iida, Y., Ilyina, T., Jacobson, A. R., Jain, A., Jarníková, T., Jersild, A., Jiang, F., Jin, Z., Joos, F., Kato, E., Keeling, R. F., Kennedy, D., Klein Goldewijk, K., Knauer, J., Korsbakken, J. I., Körtzinger, A., Lan, X., Lefèvre, N., Li, H., Liu, J., Liu, Z., Ma, L., Marland, G., Mayot, N., McGuire, P. C., McKinley, G. A., Meyer, G., Morgan, E. J., Munro, D. R., Nakaoka, S. I., Niwa, Y., O'Brien, K. M., Olsen, A., Omar, A. M., Ono, T., Paulsen, M., Pierrot, D., Pocock, K., Poulter, B., Powis, C. M., Rehder, G., Resplandy, L., Robertson, E., Rödenbeck, C., Rosan, T. M., Schwinger, J., Séférian, R., Smallman, T. L., Smith, S. M., Sospedra-Alfonso, R., Sun, Q., Sutton, A. J., Sweeney, C., Takao, S., Tans, P. P., Tian, H., Tilbrook, B., Tsujino, H., Tubiello, F., van der Werf, G. R., van Ooijen, E., Wanninkhof, R., Watanabe, M., Wimart-Rousseau, C., Yang, D., Yang, X., Yuan, W., Yue, X., Zaehle, S., Zeng, J., and Zheng, B.: Global Carbon Budget 2023, Earth Syst. Sci. Data, 15, 5301-5369, 10.5194/essd-15-5301-2023, 2023.

Gentine, P., Green, J. K., Guérin, M., Humphrey, V., Seneviratne, S. I., Zhang, Y., and Zhou, S.: Coupling between the terrestrial carbon and water cycles—a review, Environmental Research Letters, 14, 083003, 10.1088/1748-9326/ab22d6, 2019.

Gocic, M. and Trajkovic, S.: Analysis of changes in meteorological variables using Mann-Kendall and Sen's slope estimator statistical tests in Serbia, Global and Planetary Change, 100, 172-182, https://doi.org/10.1016/j.gloplacha.2012.10.014, 2013.

Gray, S. B., Dermody, O., Klein, S. P., Locke, A. M., McGrath, J. M., Paul, R. E., Rosenthal, D. M., Ruiz-Vera, U. M., Siebers, M. H., Strellner, R., Ainsworth, E. A., Bernacchi, C. J., Long, S. P., Ort, D. R., and Leakey, A. D. B.: Intensifying drought eliminates the expected benefits of elevated carbon dioxide for soybean, Nature Plants, 2, 16132, 10.1038/nplants.2016.132, 2016.

Guan, X., Li, Y., Chen, J. M., Ma, Y., and Shen, H.: A process model-guided transfer learning framework for mapping global gross primary production, Agricultural and Forest Meteorology, 372, 110678, https://doi.org/10.1016/j.agrformet.2025.110678, 2025.

Huang, L., He, B., Han, L., Liu, J., Wang, H., and Chen, Z.: A global examination of the response of ecosystem water-use efficiency to drought based on MODIS data, Science of The Total Environment, 601-602, 1097-1107, https://doi.org/10.1016/j.scitotenv.2017.05.084, 2017.

Huang, M., Zhai, P., and Piao, S.: Divergent responses of ecosystem water use efficiency to drought timing over Northern Eurasia, Environmental Research Letters, 16, 045016, 10.1088/1748-9326/abf0d1, 2021.

Huang, M., Wang, X., Keenan, T. F., and Piao, S.: Drought timing influences the legacy of tree growth recovery, Global Change Biology, 24, 3546-3559, https://doi.org/10.1111/gcb.14294, 2018.

Huxman, T. E., Smith, M. D., Fay, P. A., Knapp, A. K., Shaw, M. R., Loik, M. E., Smith, S. D., Tissue, D. T., Zak, J. C., Weltzin, J. F., Pockman, W. T., Sala, O. E., Haddad, B. M., Harte, J., Koch, G. W., Schwinning, S., Small, E. E., and Williams, D. G.: Convergence across biomes to a common rain-use efficiency, Nature, 429, 651-654, 10.1038/nature02561, 2004.

Jaramillo, F., Licero, L., Åhlen, I., Manzoni, S., Rodríguez-Rodríguez, J. A., Guittard, A., Hylin, A., Bolaños, J., Jawitz, J., Wdowinski, S., Martínez, O., and Espinosa, L. F.: Effects of Hydroclimatic Change and Rehabilitation Activities on Salinity and Mangroves in the Ciénaga Grande de Santa Marta, Colombia, Wetlands, 38, 755-767, 10.1007/s13157-018-1024-7, 2018.

Jiao, W., Wang, L., Smith, W. K., Chang, Q., Wang, H., and D'Odorico, P.: Observed increasing water constraint on vegetation growth over the last three decades, Nature Communications, 12, 3777, 10.1038/s41467-021-24016-9, 2021.

Kannenberg, S. A., Schwalm, C. R., and Anderegg, W. R. L.: Ghosts of the past: how drought legacy effects shape forest functioning and carbon cycling, Ecology Letters, 23, 891-901, https://doi.org/10.1111/ele.13485, 2020.

Keenan, T. F., Hollinger, D. Y., Bohrer, G., Dragoni, D., Munger, J. W., Schmid, H. P., and Richardson, A. D.: Increase in forest water-use efficiency as atmospheric carbon dioxide concentrations rise, Nature, 499, 324-327, 10.1038/nature12291, 2013.

Kellner, J., Houska, T., Manderscheid, R., Weigel, H. J., Breuer, L., and Kraft, P.: Response of maize biomass and soil water fluxes on elevated CO(2) and drought-From field experiments to process-based simulations, Glob Chang Biol, 25, 2947-2957, 10.1111/gcb.14723, 2019.

Klein, T., Cohen, S., and Yakir, D.: Hydraulic adjustments underlying drought resistance of Pinus halepensis, Tree Physiology, 31, 637-648, 10.1093/treephys/tpr047, 2011.

Knapp, A. K., Condon, K. V., Folks, C. C., Sturchio, M. A., Griffin-Nolan, R. J., Kannenberg, S. A., Gill, A. S., Hajek, O. L., Siggers, J. A., and Smith, M. D.: Field experiments have enhanced our understanding of drought impacts on terrestrial ecosystems—But where do we go from here?, Functional Ecology, 38, 76-97, https://doi.org/10.1111/1365-2435.14460, 2024.

Knauer, J., Zaehle, S., Medlyn, B. E., Reichstein, M., Williams, C. A., Migliavacca, M., De Kauwe, M. G., Werner, C., Keitel, C., Kolari, P., Limousin, J.-M., and Linderson, M.-L.: Towards physiologically meaningful water-use efficiency estimates from eddy covariance data, Global Change Biology, 24, 694-710, https://doi.org/10.1111/gcb.13893, 2018.

Li, D., An, L., Zhong, S., Shen, L., and Wu, S.: Declining coupling between vegetation and drought over the past three decades, Glob Chang Biol, 30, e17141, 10.1111/gcb.17141, 2024.

Li, F., Xin, Q., Green, J. K., Yi, C., Kemanian, A. R., Kannenberg, S. A., Stoy, P. C., Yang, Y., Lei, H., Xiong, Y., and Fu, Z.: Event-Specific Meteorological Drivers Shape Diverse Water-Use Efficiency Trajectories Under Drought Propagation, Global Change Biology, 32, e70690, https://doi.org/10.1111/gcb.70690, 2026.

Li, F., Xin, Q., Yi, C., Kannenberg, S. A., Green, J. K., Migliavacca, M., Moore, D. J. P., Kemanian, A. R., Gentine, P., Stoy, P. C., Zhang, F., Xiong, Y., and Fu, Z.: Limited Regulation of Canopy Water Use Efficiency by Stomatal Behavior Under Drought Propagation, Global Change Biology, 31, e70381, https://doi.org/10.1111/gcb.70381, 2025.

Li, H., Wei, M., Dong, L., Hu, W., Xiong, J., Sun, Y., Sun, Y., Yao, S., Gong, H., Zhang, Y., Hou, Q., Wang, X., Xie, S., Zhang, L., Akram, M. A., Rao, Z., Degen, A. A., Niklas, K. J., Ran, J., Ye, J.-s., and Deng, J.: Leaf and ecosystem water use efficiencies differ in their global-scale patterns and drivers, Agricultural and Forest Meteorology, 319, 108919, https://doi.org/10.1016/j.agrformet.2022.108919, 2022a.
Li, W., Migliavacca, M., Forkel, M., Denissen, J. M. C., Reichstein, M., Yang, H., Duveiller, G., Weber, U., and Orth, R.: Widespread increasing vegetation sensitivity to soil moisture, Nature Communications, 13, 3959, 10.1038/s41467-022-31667-9, 2022b.
Li, X. Y., Zou, L., Xia, J., Dou, M., Li, H. W., and Song, Z. H.: Untangling the effects of climate change and land use/cover change on spatiotemporal variation of evapotranspiration over China, Journal of Hydrology, 612, 10.1016/j.jhydrol.2022.128189, 2022c.
Liu, D., Yu, C., and Zhao, F.: Response of the water use efficiency of natural vegetation to drought in Northeast China, Journal of Geographical Sciences, 28, 611-628, 10.1007/s11442-018-1494-9, 2018.
Liu, J., Wang, Q., Zhan, W., Lian, X., and Gentine, P.: When and where soil dryness matters to ecosystem photosynthesis, Nature Plants, 11, 1390-1400, 10.1038/s41477-025-02024-7, 2025.
Liu, L., Gudmundsson, L., Hauser, M., Qin, D.-h., Li, S., and Seneviratne, S. I.: Soil moisture dominates dryness stress on ecosystem production globally, Nature Communications, 11, 2020.
Lu, X. and Zhuang, Q.: Evaluating evapotranspiration and water-use efficiency of terrestrial ecosystems in the conterminous United States using MODIS and AmeriFlux data, Remote Sensing of Environment, 114, 1924-1939, https://doi.org/10.1016/j.rse.2010.04.001, 2010.
Ma, J., Jia, X., Zha, T., Bourque, C. P. A., Tian, Y., Bai, Y., Liu, P., Yang, R., Li, C., Li, C., Xie, J., Yu, H., Zhang, F., and Zhou, C.: Ecosystem water use efficiency in a young plantation in Northern China and its relationship to drought, Agricultural and Forest Meteorology, 275, 1-10, https://doi.org/10.1016/j.agrformet.2019.05.004, 2019.
Ma, W., Li, G., Wu, J., Xu, G., and Wu, J.: Response of soil labile organic carbon fractions and carbon-cycle enzyme activities to vegetation degradation in a wet meadow on the Qinghai–Tibet Plateau, Geoderma, 377, 114565, https://doi.org/10.1016/j.geoderma.2020.114565, 2020.
Martínez-Vilalta, J., Poyatos, R., Aguadé, D., Retana, J., and Mencuccini, M.: A new look at water transport regulation in plants, New Phytol, 204, 105-115, 10.1111/nph.12912, 2014.
Maurer, G. E., Hallmark, A. J., Brown, R. F., Sala, O. E., and Collins, S. L.: Sensitivity of primary production to precipitation across the United States, Ecology Letters, 23, 527-536, https://doi.org/10.1111/ele.13455, 2020.
Miguez-Macho, G. and Fan, Y.: The role of groundwater in the Amazon water cycle: 1. Influence on seasonal streamflow, flooding and wetlands, Journal of Geophysical Research: Atmospheres, 117, https://doi.org/10.1029/2012JD017539, 2012.
Miller, D. L., Wolf, S., Fisher, J. B., Zaitchik, B. F., Xiao, J., and Keenan, T. F.: Increased photosynthesis during spring drought in energy-limited ecosystems, Nature Communications, 14, 7828, 10.1038/s41467-023-43430-9, 2023.
Mokhtar, A., Jalali, M., He, H., Al-Ansari, N., Elbeltagi, A., Alsafadi, K., Abdo, H. G., Sammen, S. S., Gyasi-Agyei, Y., and Rodrigo-Comino, J.: Estimation of SPEI Meteorological Drought Using Machine Learning Algorithms, IEEE Access, 9, 65503-65523, 2021.
Novick, K. A., Ficklin, D. L., Stoy, P. C., Williams, C. A., Bohrer, G., Oishi, A. C., Papuga, S. A., Blanken, P. D., Noormets, A., Sulman, B. N., Scott, R. L., Wang, L., and Phillips, R. P.: The increasing importance of atmospheric demand for ecosystem water and carbon fluxes, Nature Climate Change, 6, 1023-1027, 10.1038/nclimate3114, 2016.
Peters, W., van der Velde, I. R., van Schaik, E., Miller, J. B., Ciais, P., Duarte, H. F., van der Laan-Luijkx, I. T., van der Molen, M. K., Scholze, M., Schaefer, K., Vidale, P. L., Verhoef, A., Wårlind, D., Zhu, D., Tans, P. P.,

Vaughn, B., and White, J. W. C.: Increased water-use efficiency and reduced CO2 uptake by plants during droughts at a continental scale, Nature Geoscience, 11, 744-748, 10.1038/s41561-018-0212-7, 2018.
Piao, S., Wang, X., Park, T., Chen, C., Lian, X., He, Y., Bjerke, J. W., Chen, A., Ciais, P., Tømmervik, H., Nemani, R. R., and Myneni, R. B.: Characteristics, drivers and feedbacks of global greening, Nature Reviews Earth & Environment, 1, 14-27, 10.1038/s43017-019-0001-x, 2020.
Poppe Terán, C., Naz, B. S., Graf, A., Qu, Y., Hendricks Franssen, H.-J., Baatz, R., Ciais, P., and Vereecken, H.: Rising water-use efficiency in European grasslands is driven by increased primary production, Communications Earth & Environment, 4, 95, 10.1038/s43247-023-00757-x, 2023.
Reichstein, M., Bahn, M., Ciais, P., Frank, D., Mahecha, M. D., Seneviratne, S. I., Zscheischler, J., Beer, C., Buchmann, N., Frank, D. C., Papale, D., Rammig, A., Smith, P., Thonicke, K., van der Velde, M., Vicca, S., Walz, A., and Wattenbach, M.: Climate extremes and the carbon cycle, Nature, 500, 287-295, 10.1038/nature12350, 2013.
Runge, J.: Discovering contemporaneous and lagged causal relations in autocorrelated nonlinear time series datasets, Proceedings of the 36th Conference on Uncertainty in Artificial Intelligence (UAI), Proceedings of Machine Learning Research2020.
Runge, J., Bathiany, S., Bollt, E., Camps-Valls, G., Coumou, D., Deyle, E., Glymour, C., Kretschmer, M., Mahecha, M. D., Muñoz-Marí, J., van Nes, E. H., Peters, J., Quax, R., Reichstein, M., Scheffer, M., Schölkopf, B., Spirtes, P., Sugihara, G., Sun, J., Zhang, K., and Zscheischler, J.: Inferring causation from time series in Earth system sciences, Nature Communications, 10, 2553, 10.1038/s41467-019-10105-3, 2019.
Schwalm, C. R., Williams, C. A., Schaefer, K., Baldocchi, D., Black, T. A., Goldstein, A. H., Law, B. E., Oechel, W. C., Paw U, K. T., and Scott, R. L.: Reduction in carbon uptake during turn of the century drought in western North America, Nature Geoscience, 5, 551-556, 10.1038/ngeo1529, 2012.
Seddon, A. W. R., Macias-Fauria, M., Long, P. R., Benz, D., and Willis, K. J.: Sensitivity of global terrestrial ecosystems to climate variability, Nature, 531, 229-232, 10.1038/nature16986, 2016.
Smith, T. and Boers, N.: Global vegetation resilience linked to water availability and variability, Nature Communications, 14, 498, 10.1038/s41467-023-36207-7, 2023.
Tang, J., Niu, B., Hu, Z., and Zhang, X.: Increasing susceptibility and shortening response time of vegetation productivity to drought from 2001 to 2021, Agricultural and Forest Meteorology, 352, 110025, https://doi.org/10.1016/j.agrformet.2024.110025, 2024.
Trenberth, K. E., Dai, A., van der Schrier, G., Jones, P. D., Barichivich, J., Briffa, K. R., and Sheffield, J.: Global warming and changes in drought, Nature Climate Change, 4, 17-22, 10.1038/nclimate2067, 2014.
Vicente-Serrano, S. M., Gouveia, C., Camarero, J. J., Beguería, S., Trigo, R., López-Moreno, J. I., Azorín-Molina, C., Pasho, E., Lorenzo-Lacruz, J., Revuelto, J., Morán-Tejeda, E., and Sanchez-Lorenzo, A.: Response of vegetation to drought time-scales across global land biomes, Proc Natl Acad Sci U S A, 110, 52-57, 10.1073/pnas.1207068110, 2013.
Vicente-Serrano, S. M., Gouveia, C. M., Camarero, J. J., Beguería, S., Trigo, R. M., López-Moreno, J. I., Azorín-Molina, C., Pasho, E., Lorenzo-Lacruz, J., Revuelto, J., Morán-Tejeda, E., and Sanchez-Lorenzo, A.: Response of vegetation to drought time-scales across global land biomes, Proceedings of the National Academy of Sciences, 110, 52 - 57, 2012.
Walther, S., Duveiller, G., Jung, M., Guanter, L., Cescatti, A., and Camps-Valls, G.: Satellite Observations of the Contrasting Response of Trees and Grasses to Variations in Water Availability, Geophysical Research Letters, 46, 1429-1440, https://doi.org/10.1029/2018GL080535, 2019.
Wang, C., Min, L., Zhang, J., Li, Y., Liu, X., Lü, Y., Feng, X., and Fu, B.: Vegetation restoration dominates increase in water use efficiency in drylands of China, Ecological Indicators, 145, 109703, https://doi.org/10.1016/j.ecolind.2022.109703, 2022.

Wang, M., Ding, Z., Wu, C., Song, L., Ma, M., Yu, P., Lu, B., and Tang, X.: Divergent responses of ecosystem water-use efficiency to extreme seasonal droughts in Southwest China, Science of The Total Environment, 760, 143427, https://doi.org/10.1016/j.scitotenv.2020.143427, 2021.

Wang, X., Fu, Z., Ciais, P., Peñuelas, J., Xiao, J., Li, X., Luo, X., Chen, C., Xia, H., Zhou, T., Stoy, P. C., Green, J. K., and Zhang, F.: Multi-satellite derived data reveals spatiotemporal dynamics of carbon-water coupling and its drivers in tropical ecosystems, Remote Sensing of Environment, 334, 115242, https://doi.org/10.1016/j.rse.2026.115242, 2026a.

Wang, X., Fu, Z., Ciais, P., Wang, L., Buchmann, N., Keenan, T. F., De Kauwe, M., Peñuelas, J., Chen, G., Gong, X., Xiao, J., Li, X., Xie, Q., Stoy, P. C., Makowski, D., Smith, W. K., Wang, H., Wang, S., Zhang, F., and Niu, S.: Global distribution and changes of leaf-level intrinsic water use efficiency and their responses to water stress, Nature Communications, 17, 1530, 10.1038/s41467-025-68252-9, 2026b.

Wang, Z., Wu, R., Li, J., Liu, Y., Cui, C., and Liu, J.: Discriminating the impact of soil moisture and vapor pressure deficit on vegetation greening over multiple time scales, Global and Planetary Change, 255, 105111, https://doi.org/10.1016/j.gloplacha.2025.105111, 2025.

Wang, Z., Fu, B., Wu, X., Li, Y., Feng, Y., Wang, S., Wei, F., and Zhang, L.: Vegetation resilience does not increase consistently with greening in China's Loess Plateau, Communications Earth & Environment, 4, 336, 10.1038/s43247-023-01000-3, 2023.

Wen, Y., Liu, X., Xin, Q., Wu, J., Xu, X., Pei, F., Li, X., Du, G., Cai, Y., Lin, K., Yang, J., and Wang, Y.: Cumulative Effects of Climatic Factors on Terrestrial Vegetation Growth, Journal of Geophysical Research: Biogeosciences, 124, 789-806, https://doi.org/10.1029/2018JG004751, 2019.

Wilson, K. B., Carlson, T. N., and Bunce, J. A.: Feedback significantly influences the simulated effect of CO2 on seasonal evapotranspiration from two agricultural species, Global Change Biology, 5, 903-917, https://doi.org/10.1046/j.1365-2486.1999.00280.x, 1999.

Winkler, K., Fuchs, R., Rounsevell, M., and Herold, M.: Global land use changes are four times greater than previously estimated, Nature Communications, 12, 2501, 10.1038/s41467-021-22702-2, 2021.

Wu, R., Wang, Z., Meng, F., Liu, Y., and Shi, H.: Strengthening Coupling Between Vegetation and Soil-Atmosphere Compound Drought Over the Past Two Decades, Earth's Future, 13, e2025EF006311, https://doi.org/10.1029/2025EF006311, 2025.

Xie, J., Zha, T., Zhou, C., Jia, X., Yu, H., Yang, B., Chen, J., Zhang, F., Wang, B., Bourque, C. P. A., Sun, G., Ma, H., Liu, H., and Peltola, H.: Seasonal variation in ecosystem water use efficiency in an urban-forest reserve affected by periodic drought, Agricultural and Forest Meteorology, 221, 142-151, https://doi.org/10.1016/j.agrformet.2016.02.013, 2016.

Xue, Y., Liang, H., Zhang, B., and He, C.: Vegetation restoration dominated the variation of water use efficiency in China, Journal of Hydrology, 612, 128257, https://doi.org/10.1016/j.jhydrol.2022.128257, 2022.

Yan, W., Zhou, J., Lin, H., Luo, J., Duan, X., and Wu, R.: Drivers of the pre-season drought thresholds triggering earlier autumn foliar senescence in the Northern Hemisphere, Nature Communications, 16, 7568, 10.1038/s41467-025-62847-y, 2025a.

Yan, Y., Li, B., Dechant, B., Xu, M., Luo, X., Qu, S., Miao, G., Leng, J., Shang, R., Shu, L., Jiang, C., Wang, H., Jeong, S., Ryu, Y., and Chen, J. M.: Plant traits shape global spatiotemporal variations in photosynthetic efficiency, Nature Plants, 11, 924-934, 10.1038/s41477-025-01958-2, 2025b.

Yang, S., Zhang, J., Han, J., Bai, Y., Xun, L., Zhang, S., Cao, D., and Wang, J.: The ratio of transpiration to evapotranspiration dominates ecosystem water use efficiency response to drought, Agricultural and Forest Meteorology, 363, 110423, https://doi.org/10.1016/j.agrformet.2025.110423, 2025.

Yang, Y., Guan, H., Batelaan, O., McVicar, T. R., Long, D., Piao, S., Liang, W., Liu, B., Jin, Z., and Simmons, C. T.: Contrasting responses of water use efficiency to drought across global terrestrial ecosystems, Scientific Reports, 6, 23284, 10.1038/srep23284, 2016.

Zeng, X., Hu, Z., Chen, A., Yuan, W., Hou, G., Han, D., Liang, M., Di, K., Cao, R., and Luo, D.: The global decline in the sensitivity of vegetation productivity to precipitation from 2001 to 2018, Global Change Biology, 28, 6823-6833, https://doi.org/10.1111/gcb.16403, 2022.

Zhang, H., Zhang, Y., Miralles, D. G., Tai, X., Koppa, A., Yang, H., Sitch, S., and O'Sullivan, M.: Increase in plant reliance on past precipitation associated with greening and drying, Nature Ecology & Evolution, 10.1038/s41559-026-02997-4, 2026.

Zhang, Y., Gentine, P., Luo, X., Lian, X., Liu, Y., Zhou, S., Michalak, A. M., Sun, W., Fisher, J. B., Piao, S., and Keenan, T. F.: Increasing sensitivity of dryland vegetation greenness to precipitation due to rising atmospheric CO2, Nature Communications, 13, 4875, 10.1038/s41467-022-32631-3, 2022.

Zhao, T., Zhang, Y., Zhang, T., Xu, M., Zhu, J., He, Y., and Yu, G.: Drought occurrence and time-dominated variations in water use efficiency in an alpine meadow on the Tibetan Plateau, Ecohydrology, 15, e2360, https://doi.org/10.1002/eco.2360, 2022.

Zhou, Z., Wang, P., Li, L., Fu, Q., Ding, Y., Chen, P., Xue, P., Wang, T., and Shi, H.: Recent development on drought propagation: A comprehensive review, Journal of Hydrology, 645, 132196, https://doi.org/10.1016/j.jhydrol.2024.132196, 2024.